ACS OMEGA

Article

Impact of Oil-Prone Sedimentary Organic Matter Quality and Hydrocarbon Generation on Source Rock Porosity: Artificial Thermal Maturation Approach

Amélie Cavelan, Mohammed Boussafir,* Claude Le Milbeau, and Fatima Laggoun-Défarge

Read Online

ACCESS | Metrics & More | Article Recommendations | Supporting Information

ABSTRACT: This work investigates the relation between the molecular composition of the organic matter (OM), hydrocarbon generation, and porosity of artificially matured mudstones from the Kimmeridge Clay formation. Anhydrous thermal maturations, geochemical characterization (gas chromatography−mass spectrometry, gas chromatography with a thermal conductivity detector), scanning electron microscopy observations, and nitrogen adsorption measurements were carried out. The results were compared to the calculated OM porosity after maturation. Our results reveal that samples richer in phytoplanktonic OM generated

more abundant oils enriched in alkanes and lighter aromatic hydrocarbons (i.e., biphenyls and naphthalenes) that are more able to fill the adjacent pores of the mineral matrix during maturation. Both the calculated and the observed OM porosity increases during maturation, but the measured rock pore volume shows a non-linear evolution related to the amount of gas generated and the ensuing ability of the rock to preserve the pores. The secondary cracking of highly oil-prone samples generated larger amounts of C_1-C_5 gases but lower pore volumes, less well preserved. OM composition and its ability to generate oil and gas seem therefore to affect the pore volume. These variations are nevertheless small compared to the effect of thermal maturity, which remains the major process controlling the evolution of porosity. During gas generation, high C_2-C_5 concentrations are generated compared to methane. The short thermal maturation duration of our experiments may have delayed the conversion of C_2-C_5 hydrocarbons to methane. In addition, slight differences in the concentrations of saturated and aromatic components and markedly different pore volumes and pore size distributions exist between artificially and naturally matured rocks. The conditions of artificial maturations may thus impact the thermal transformations of OM, emphasizing the necessity to investigate the role of the artificial maturation kinetics on OM and porosity.
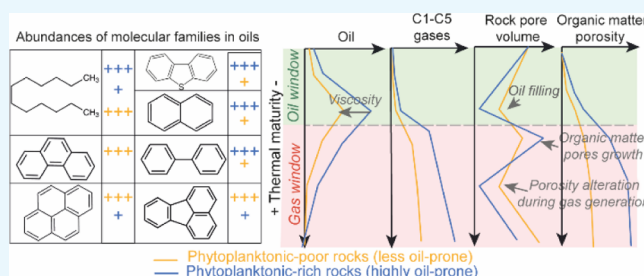
■ INTRODUCTION

The increase in thermal maturity with burial and sedimentary organic matter (OM) thermal degradation processes is widely considered as the main factor controlling the development of pores in organic-rich mudstones.[1−7] While the interparticle porosity has been thought to decrease with burial because of structural rearrangements under compaction and possible occlusion by entrapped bitumen,[6,8] the OM-hosted porosity, predominant in many reservoirs, generally increases with increasing depth.[1,4,5,8−12] However, because of the concomitant effect of many other parameters (mineralogy and the associated rock framework, OM content and composition), the relation between thermal maturity, OM molecular thermal transformations, and porosity is not always clear.[5,10,13−18] Models exist to estimate the OM porosity (OMp).[8] For these models, the OMp depends on the organic richness, the oil generation potential, and thermal maturity of the rock.[8] Nevertheless, Fishman et al.[13] and Wang et al.[19] suggested that the stability of the OM-hosted porosity and the ability of the rock to preserve the pores are closely related to the mineralogy

and the rock fabric. Hence, they proposed that OM-hosted pores are likely to be better preserved in silica or calcite-rich formations than in ductile clay-rich formations. In accordance with Milliken et al.[16] and Pan et al.,[17] Wang et al.[19] proposed also that the organic richness may significantly influence the ability of rocks to preserve pores from compaction during burial. Some evidence suggests also that the impact of thermal maturity on porosity depends on the original OM composition, maceral types, and the OM distribution in rocks.[5,10,20−24]
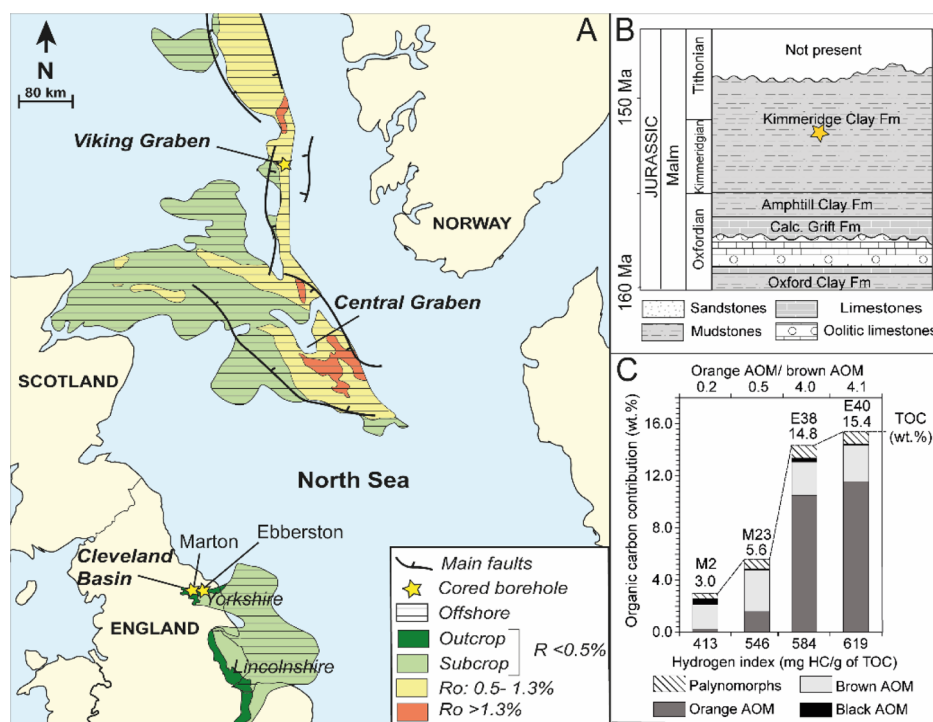
Sedimentary OM can be composed of particles of various origins, with distinct morphologies, internal structure, and chemical composition. Variations in the abundance of these individual OM types may influence the timing and the ability

Figure 1. (A) Location of the studied boreholes in the KCF. (B) Stratigraphy of the Cleveland basin. (C) Palynofacies composition, TOC, hydrogen index (Rock Eval 6 HI), and orange/brown AOM of the studied samples. Modified from Cavelan et al.[21] Palynomorphs: phytoclasts, pollen, spores, preserved phytoplankton, and algal fragments. AOM: amorphous organic matter.

to generate oil, gas, and solid bitumen during burial.[25] This may lead to variation in the character, the distribution, and the timing at which pores are generated during maturation. For example, Ko et al.[10] showed that the different abundance of *Tasmanites* between the Eagle Ford and Barnett mudstones has an impact on the pore evolution models with increasing maturity. Our previous work on the Kimmeridge Clay Formation (KCF)[21] showed that slight variations in the maceral composition in the same type II OM can influence the evolution of porosity of organic-rich mudstones during thermal maturation. Wood et al.[26] suggests that variations of the initial composition of solid bitumen/pyrobitumen can be at the origin of the variations of porosity and texture observed in different pyrobitumen particles in the Montney Formation. However, while the evolution of the molecular composition of OM as a function of both the OM origin and thermal maturity have been well-documented,[25,27−34] the influence of the composition of bitumen and gas generated during maturation on source rock porosity remains poorly understood. The use of molecular OM geochemical analyses could thus be the key to better understanding the relations existing between slight variations of a same type II OM original composition, its thermal transformations, the composition of bitumen and gas, and porosity during thermal maturation.

To this end, laboratory anhydrous thermal maturations, molecular geochemical characterization [gas chromatography−mass spectrometry (GC−MS) and gas chromatography with a thermal conductivity detector (GC/TCD)], and nitrogen adsorption measurement were applied to immature samples from the KCF (Yorkshire, UK). Previous works demonstrated that under the high temperatures of laboratory experiments, hydrous conditions may modify the ability of water to enter the OMp, affecting the OM thermal degradation.[35,36] According to these results, anhydrous artificial maturation conditions were

used (no water was added in gold cells during the experiments). The results of our anhydrous maturations were then compared with naturally matured rocks from the Viking Graben (Kimmeridge Clay Fm.) and the Vaca Muerta formation (VMF) to assess the representativeness of our maturation experiments. Then, the OMp of artificially matured KCF samples was calculated using the model of Modica and Lapierre[8] and compared to the measured total rock pore volume after maturation. The main objective of this work is to isolate the link between the molecular composition of the effluents generated during maturation and variations in the pore volume of Kimmeridge Clay source rocks during artificial maturation.

MATERIALS AND METHODS

Samples. The six immature marine mudstones for anhydrous thermal maturations were sampled in Marton and Ebberston boreholes in the KCF of the Cleveland Basin (Pickering Vale, Yorkshire, UK, Figure 1) between 128.15−128.78 and 69.98−70.28 m deep, respectively. This geological section was well presented in previous works.[37−43] The studied rocks consist of finely laminated immature organic-rich marine mudstones (vitrine reflectance ≈ 0.48%[21]) internally marked by rhythmic variations in both OM content and OM oil-prone quality which reflect cyclic climatic and eustatic variations.[42,44,45] The OM is mainly composed of three distinct types of marine amorphous organic matter (AOM) (orange, brown, and black AOM in the order of decreasing abundance), with a minor contribution of plant tissues and zooplankton.[39,42,43] The relatively low-total organic carbon (TOC) mudstones are dominated by brown AOM[38] and exhibit a lower oil-generation potential. The relatively high-TOC mudstones are characterized by higher contents of orange AOM consisting of highly oil-prone phytoplanktonic

OM.[39,42,45] To cover slightly different OM oil-prone quality, six samples were selected in the whole cycle. Only the four most representative samples are entirely described in this work (the most intermediate OM contents and compositions of the series, Figure 1).

Previous works on the studied samples[21,43] showed that M2 and M23 contain low amounts of orange AOM, a higher relative proportion of brown AOM (Or/br AOM ≤ 1.3), and a slightly lower oil-generation potential [hydrogen index (HI) = 413−546 mg HC/g of TOC]. E40 and E38 exhibit high oil-prone orange AOM contents with a lower relative proportion of brown AOM (Or/br AOM ranging from 2.4−4.1) and a slightly higher oil-generation potential (HI = 584−599 mg HC/g of TOC, Figure 1).[21,43] The intermediate samples M31 and E19 exhibit HI of 574 and 557 mg HC/g of TOC, respectively.[21] The relative abundance (in %) of each type of particles present in total isolated OM (considered equivalent to the TOC) was measured on isolated OM (obtained by classical HF and HCl treatments) using transmitted light and under oil immersion. According to the TOC (Rock Eval 6 TOC, wt %) of each sample, these values were then converted into an organic carbon contribution (in wt %).[21]

In order to compare the results from artificial maturation experiments with natural samples, two gas-mature mudstones were selected in the VMF (VMF1 and 2, Aguada Pichana borehole, Neuquén basin, Argentina) at 2668 and 2769 m deep, and one oil-mature KCF sample was obtained from the Viking Graben, VK1 (south-east Norwegian coast, North Sea, Figure 1) at 3913 m deep. The Vaca Muerta is often considered as a good time equivalent of the KCF in terms of OM composition (similar type II OM precursor dominated by marine algal AOM with variable amounts of marine microplankton and terrestrial materials).[46,47] Except differences of maturity in petrographic observations, VK1 is very similar to the sample M2 in terms of OM distribution and maceral composition.

Thermal Maturation. About 1 g of the six total powdered (≈250 μm of grain size) immature KCF mudstones was oven-dried 12 h at 105 °C. The atmospheric adsorbed water content can vary between samples causing differences in maturation processes which are not related to the OM composition. The samples were dried in order (i) to homogenize the initial conditions of samples and (ii) to reach the water content corresponding to the interlayer water of clay minerals. The cells were then placed inside gold cells (55 mm × 5 mm) and sealed under an argon atmosphere. The sealed cells were introduced into high-pressure stainless-steel autoclaves pressurized at 600 bars with water and inserted into pyrolysis ovens for anhydrous confined thermal maturation. No water was added in the cell during experiments, but water can be naturally generated during the thermal cracking of OM and clay minerals diagenetic transformations. The temperature of the system was raised at 4.5 °C min^{-1} to the final temperature. The samples were isothermally heated at 325, 350, 390, 440, and 470 °C for 72 h. The oven was then turned off, and the autoclaves were slowly depressurized. The same experiments were carried out on small cores (1 cm × 0.45 mm) of the same KCF samples in order to make bulk polished rock sections for petrographic observations.

Organic Geochemistry. After maturation, the gold cells were sealed in glass bottles (25 cm^3) and pierced under vacuum. Gases (2 cm^3) were sampled in the bottle with a gastight syringe and injected in a GC/TCD. Gas composition was determined using a PerkinElmer Clarus 580 gas chromatograph (for the operating conditions see the Supporting Information). Gas concentration was quantified by assuming ideal gas behavior using peak area integrations compared with calibration curves.

Total powdered and dried KCF mudstones (50−60 mg) were analyzed using a new Rock-Eval 6 (Vinci Technologies) pyrolizer before and after maturation to determine the TOC, the S_2 [hydrocarbons (HCs) generated during pyrolysis], and oil-generation potential (HI, mg/g of TOC). The significance of these parameters was explained by Espitalie et al.[48,49] and Lafargue et al.[50] (operating conditions in Supporting Information).

To enable extraction of the lipidic components before and after thermal maturation, ≈1 g of total pulverized samples was extracted with a dichloromethane/methanol (1/1) mixture using ultrasonication. The extracts were desulfurized on copper and were separated by a deactivated silica gel (5% with water) chromatography column. Elution with heptane recovered the aliphatic fractions (SAT). Subsequent elution with a mixture of heptane/toluene (3/1) and (2/2) recovered the aromatic fractions (ARO). Finally, the polar fraction was recovered by elution with methanol. The quantity of asphaltenes was calculated by mass difference between the total extract and the sum of ARO, SAT, and the polar fractions. Asphaltenes were counted with the polar fraction to obtain the total NSO fraction (nitrogen, sulfur and oxygen-rich compounds). The SAT and ARO fractions were analyzed by gas chromatography−-mass spectrometry (GC−MS) (Trace-GC Ultra gas chromatograph equipped with a Thermo Trace-Gold 5 MS capillary column coupled to a TSQ Quantum XLS mass spectrometer and fitted with an AS 3000 auto sampler, for the operating conditions see the Supporting Information). SAT and ARO compounds were identified by comparing the mass spectra and retention times with available published data. The calculation of concentrations and molecular ratios of SAT and ARO compounds were based on peak area integrations. Squalane was used as internal standard.

Thermal Maturity Assessment. Equivalent vitrinite reflectance values (R_c, %) were determined using three equations based on the methylphenanthrene index (MPI-1), the dimethylphenanthrene ratio (DPR), and the methyldibenzothiophene ratio (MDBT)[28,51] (see Appendix 1). The mean R_c represents the mean of the values obtained by these different equations. Phenanthrenes (Phes), dibenzothiophenes (DBTs), and their methylated derivatives were quantified using the peak area on ion specific chromatograms (m/z 178 + 192 + 206 and m/z 184 + 198 + 212 respectively) to avoid possible coelutions. Measurements of mean vitrinite reflectance (R_m) were carried out in order to confirm the calculated vitrinite reflectance when possible. Measurements were carried out using a microscope equipped with a photometer and an oil-immersion objective. Each mean reflectance value was determined using at least 50 random measurements carried out on polished rock sections. Calibrations were carefully made using glass-reflectance standards.[52,53] Because of the very low content of vitrinite in the samples, only a few vitrinite reflectance values can be measured to ensure the validity of R_c calculated using polyaromatic components.

Pore Size Distribution. The pore size distribution (PSD) and the total rock pore volume were measured by low-pressure nitrogen adsorption before and after thermal maturation (Quantachrome NOVA 2200^e). For analyses, samples were

Table 1. TOC, HI, Measured (R_m) and Calculated (R_c) Vitrinite Reflectance, TR, Cc, Calculated OMp, Total Pore Volume (V_{tot}) and Corresponding Porosity (P) Accessible to Nitrogen Measurements, Relative Contribution of Macro- (>50 nm), Meso- (2−50 nm), and Micropores Volume (<2 nm) (Pore Size Definition after Sing[57]) of Naturally Matured Rocks (VK1 and VMF) and Artificially Matured Mudstones at Different Maturation Temperatures (Calculated from the BJH Cumulative Pore Volume at 2 and 50 nm in Diameter, Respectively)[a]

sample name		TOC (wt %)	HI (mg/g TOC)	R_m (%)	Dev	N	R_c (%)	Dev	TR (%)	Cc (%)	OMp (%)	V_{tot} (cm³/g)	V_{macro} (%)	V_{meso} (%)	V_{micro} (%)	P (%)
VK1		2.2	292	0.85	0.08	70	0.76	0.04				3.2×10^{-2}	21.2	71.2	7.6	6.0
VMF1		5	43	1.65	0.05	50						3.5×10^{-2}	28	72	0	6.5
VMF2		6.7	19	1.69	0.1	50						3.5×10^{-2}	33.5	66.5	0	6.5
M2	raw	3.0	413	0.42	0.03	50	0.47	0.03				3.6×10^{-2}	22	74.3	3.7	6.7
M23		5.6	546	0.4	0.04	50	0.45	0.04				3.7×10^{-2}	18	78	4	6.9
E38		14.8	584	0.43	0.03	52	0.48	0.02				2.8×10^{-2}	24	72.6	3.4	5.2
E40		15.4	619				0.51	0.04				3.2×10^{-2}	34	63.2	2.8	6.0
M2	325 °C	2.9	314				0.72	0.08	27	34	0.6	1.4×10^{-2}	42	58	0	2.6
M23		5.2	471	0.66	0.04	50	0.71	0.06	20	50	1.3	1.8×10^{-2}	46	54	0	3.4
E38		14.2	556				0.70	0.03	9	61	1.8	4.9×10^{-3}	8	92	0	0.9
E40		15.2	553				0.68	0.09	12	66	2.8	5.2×10^{-3}	65	35	0	1.0
M2	350 °C	2.6	296				0.79	0.07	38	34	0.9	2.7×10^{-3}	0.3	80.7	19.3	0.5
M23		4.3	451				0.87	0.09	37	50	2.4	5.2×10^{-4}	0	84.1	15.9	0.1
E38		14.6	519				0.84	0.08	12	61	2.6	4.6×10^{-3}	0	80.8	19.2	0.9
E40		14.8	514				0.85	0.11	20	66	4.8	4.3×10^{-3}	0.4	77.4	22.2	0.8
M2	390 °C	2.2	91				1.22	0.06	84	34	2.0	1.7×10^{-2}	51	49	0	3.2
M23		3.0	187	1.4	0.08	52	1.27	0.02	82	50	5.4	1.8×10^{-2}	59.1	40.9	0	3.4
E38		13.0	155				1.20	0.03	77	61	16.1	3.4×10^{-2}	0	98	2.3	6.4
E40		13.9	189				1.22	0.07	72	66	17.1	4.6×10^{-2}	0	79.1	20.9	8.6
M2	440 °C	2.3	13				1.61	0.18	98	34	2.3	1.2×10^{-2}	0	86.1	13.9	2.2
M23		2.9	21				1.58	0.15	98	50	6.4	1.7×10^{-2}	0	86.4	13.6	3.2
E38		11.2	23				1.88	0.29	97	61	20.4	1.3×10^{-2}	0	82.2	17.8	2.4
E40		11.4	50				1.72	0.24	94	66	22.2	4.8×10^{-3}	0	78.3	21.7	0.9
M2	470 °C	2.0	10				2.50	0.16	98	34	2.3	5.3×10^{-2}	33	67	0	9.9
M23		2.8	7	2.02	0.1	50	2.50	0.18	99	50	6.5	9.2×10^{-2}	42	58	0	17.2
E38		5.9	22				2.50	0.20	98	61	20.7	3.3×10^{-2}	15.7	83.2	1.1	6.2
E40		5.4	28				2.45	0.11	98	66	23.3	6.0×10^{-2}	13.2	84.7	2.1	11.2

[a]N: number of measured vitrinite reflectance values. SAT + ARO concentrations are positively correlated with the initial content of orange AOM after heating at 350 °C ($R^2 \geq 0.97$, Figure 4A).

crushed into grains (<250 μm), oven-dried at 110 °C overnight, and outgassed in the apparatus at 105 °C for 24 h. Isotherms were obtained at 77 K (temperature of liquid nitrogen). Total pore volumes (V_{tot}) were determined after the liquid molar volume adsorbed at $P/P_0 \approx 0.987$ which is the ratio of absolute gas pressure (P) to saturation pressure (P_0) of nitrogen at 77 K (101.3 kPa). To avoid tensile strength effect phenomenon during desorption, the PSD were determined using the Barrett, Johner, and Halenda (BJH) method applied from the adsorption isotherm.[54]

Scanning Electron Microscopy Observations. Scanning electron microscopy (SEM) observations were carried out on bulk polished rock sections of the artificially matured KCF rocks. Before SEM observations, the rock sections were prepared by mechanical polishing perpendicular to bedding to facilitate broad beam argon-ion milling. The rock sections were then argon-ion milled at 1 h at 5 kV and then 30 min at 2 kV (current set as 220 μA). The sections were coated with carbon and fixed to SEM stubs with a carbon paste to improve image quality in preventing electrostatic charging effects (more details in the Supporting Information).

Estimation of OMp and Nitrogen Adsorption Porosity. The OMp of KCF samples after maturation was calculated using the method reported by Modica and Lapierre.[8] They considered that the OMp appears and then increases during thermal maturation in response to HC generation. They assumed that the OMp depends on the TOC, the transformation ratio (TR) at a given maturity, and the percent of convertible organic carbon (Cc) of a source rock according to the eq 1

$$\text{OMp} = [(\text{TOCi} \times \text{Cc}) \times k] \times \text{TR} \times \left(\frac{d_R}{d_{OM}} \right) \quad (1)$$

With TOCi the TOC of immature samples; d_R the average bulk mudstone density (~2.5 g/cm³); d_{OM}, the average density of KCF kerogen (~1.2 g/cm³);[55] and k a dimensionless scale factor corresponding to the mass of kerogen from a labile carbon mass. k was set as 1.118 based on the assumption that (i) ~95% of the TOCi is from kerogen and (ii) a convertible carbon mass represents ~85% of a convertible kerogen mass (k = 0.95/0.85 = 1.118).[8] TR was calculated according to Bordenave et al.[52] using the proportion of Rock Eval S_2 (HCs generated during Rock Eval pyrolysis under inert gas) lost after maturation (see Appendix 1, S_2 values are in Supporting Information). Cc (%) represents the original organic carbon content of a sample that can be converted into HCs during maturation. Each artificially matured sample comes from a same original immature sample thermally matured at different temperatures. We thus assumed that the Cc is the same for each sample whatever their thermal maturities because they
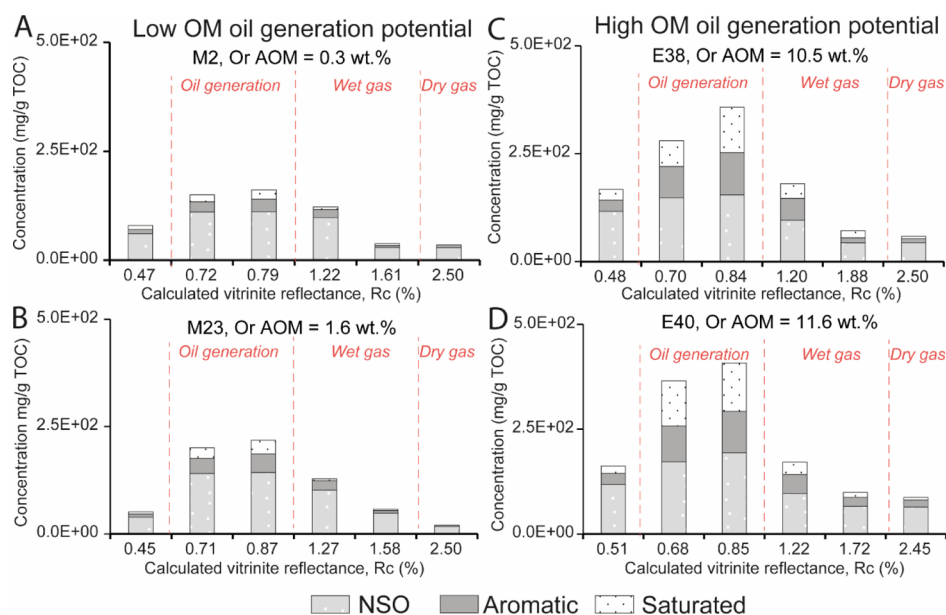
Figure 2. Variations in aromatic, saturated, and NSO concentrations in artificially matured samples with increasing maturity of samples (A) M2, (B) M23, (C) E38, and (D) E40. The initial orange amorphous organic matter (Or AOM) content increases form (A) to (D). Divisions of HCs generation stages (dashed red lines) are based on R_c, Rock Eval parameters, and corresponding data from the literature.[29]

initially come from a same rock with the same original convertible carbon content. Cc was calculated according to Modica and Lapierre[8] (see Appendix 1) using the TR and the proportion of TOC lost after reaching the higher thermal maturity stage (470 °C for 72 h). Because of the greater difference in TOC, the calculated Cc is the most accurate after this higher thermal maturation.[8,52]

For comparison with the OMp, the porosity corresponding to the pore volume measured with nitrogen adsorption was estimated using the following assumptions. According to previous studies on the KCF, the mean bulk density (δ_b) (oven dry) of the studied KCF samples is ≈1.87 cm³/g.[43] Please note that we make the assumptions that the density of the samples is relatively constant during maturation, which is probably not accurate. The mean volume of the solid phase (V_s) can be estimated by the eq 2

$$V_s = \frac{1}{\delta_b} = \frac{1}{1.87} = 0.54 \text{ cm}^3 \qquad \text{for 1 g of sample} \tag{2}$$

Then, the pore volume (V_{tot}) of nitrogen adsorption measurements gives the volume of the voids accessible to nitrogen for 1 g of sample. An estimation of the corresponding porosity (P) can thus be determined using the eq 3

$$P (\%) = \frac{V_{tot}}{V_s} \times 100 \qquad \text{for 1 g of sample} \tag{3}$$

■ RESULTS

Thermal Maturity. Before maturation, the calculated (R_c) and the measured (R_m) vitrinite reflectance of KCF samples is ≈0.48 and ≈0.42% respectively (Table 1). The R_c reaches 0.70% after maturation at 325 °C. The R_m exhibits a similar value: 0.66%. After maturation at 350, 390, 440, and 470 °C, the R_c reaches 0.84, 1.23, 1.70, and 2.48%, respectively. After heating at 390 and 470 °C, the R_m reaches 1.40 and 2.02%. The R_c of VK1 is ≈0.76% and the R_m is ≈0.85%. The R_m of VMF samples is ≈1.67%, the R_c is unquantifiable (no Phe and

DBT). The division of HC generation stages used in the different figures was done according to the correspondence between the time/temperature pairs used for artificial thermal maturation and the degree of thermal maturity currently reached in the literature.[27,29,56] This first division was then completed with R_c values, biomarker ratios, and Rock Eval parameters. The R_m served as a complement to verify the correspondence between these maturity indicators.

Extractible OM and Rock Eval Parameters. The extractible OM (EOM) content, which is low (≤165 mg/g TOC) in KCF samples before maturation, is mainly composed of NSO (Figures 2 and 3). The SAT + ARO fraction accounts for less than 25% of the EOM. After heating at 325 °C and 350 °C, EOM, SAT, and ARO concentrations and the relative
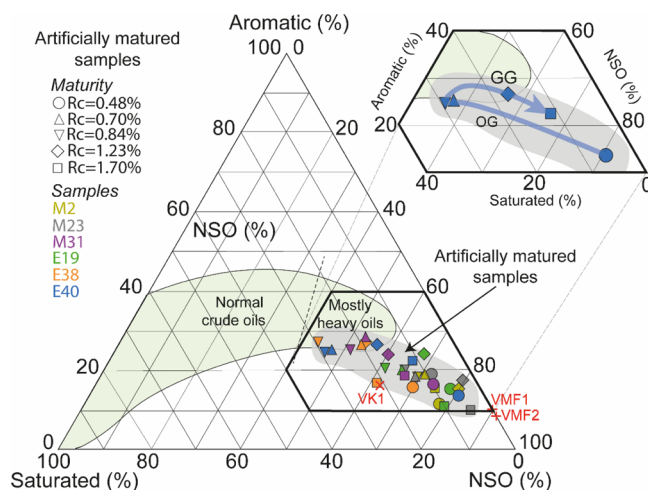
Figure 3. Relative proportion of saturated, aromatic, and NSO of naturally (VMF, VK1, in red) and artificially matured samples. Zoom on the trend followed by the most oil-prone sample during oil (OG) and gas generation (GG). Data of normal crude-oil from Tissot and Welte.[25]
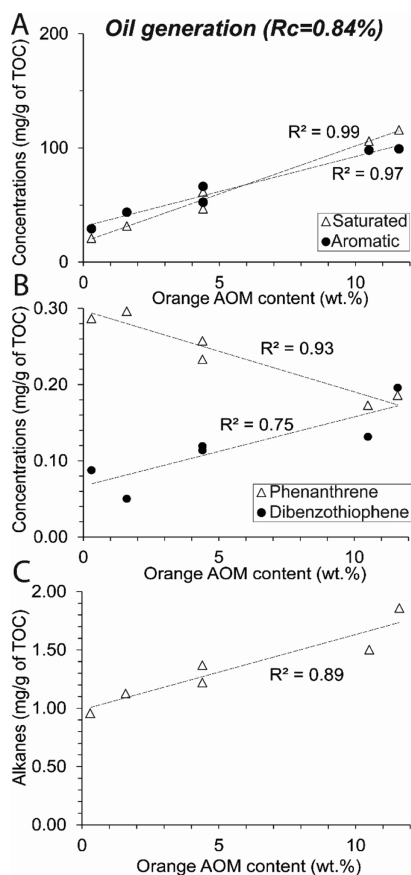
Figure 4. Evolution of (A) saturated, aromatic HC, (B) Phe, DBT, and (C) alkane concentrations of the solvent extract with increasing initial orange AOM content after artificial thermal maturation of KCF samples (oil generation, 350 °C/72 h).

proportion of SAT and ARO increase while the HI decreases (Table 1, Figures 2 and 3). The EOM generated from the highly oil-prone samples (M31, E38, E40) appears thus significantly enriched in SAT and ARO (R_c = 0.84%, Figure 3). The runs at 390, 440, and 470 °C are characterized by the decrease in EOM, SAT, and ARO concentrations (Figure 2). The relative proportion of SAT and ARO decreases (Figure 3).

Biomarkers. Normal alkanes, steranes, and hopanes are the prominent components of the SAT before maturation (≥ 0.50 mg/g of TOC, Figure 6) in the KCF. Isoprenoid alkanes, alkylcycloalkanes, and methyl-alkanes are present in low amounts (alkanes distribution in the Supporting Information). Normal alkanes extend from C_{17} to C_{38} with a distribution maximizing at C_{23} and high Pr/Ph (≈ 0.96), Pr/n-C_{17} (≈ 2.60) and Ph/n-C_{18} ratios (≈ 1.95, Figures 6 and 7).

Only a few $\leq C_{14}$ n-alkanes are present in immature samples. The hopane series extends from C_{27} to C_{35}. The regular sterane series extend from C_{21} to C_{30}. Triaromatic steroids (TASs) and C-ring monoaromatic steroids (MASs) are predominant in ARO (Figure 6, distributions of TAS, MAS, hopanes and steranes in the Supporting Information). DBTs, Phes, and their methylated derivatives are present in low amounts before maturation (≤ 0.02 mg/g of TOC, Figure 6). Samples with high orange AOM contents exhibit higher hopane, sterane, and MAS concentrations (Figure 6). These rocks exhibit lower Pr/n-C_{17} (≤ 2.24) and higher Ph/n-C_{18} (≥ 2.29) and thus display a typical type II algal marine OM signal, deposited under reducing conditions (M31, E38, E40, Figure 7B). These

samples contain also higher concentrations of n-alkanes (Figure 6). The samples poor in orange AOM exhibits higher Pr/n-C_{17} (≥ 3.01) and lower Ph/n-C_{18} (≤ 1.48) corresponding to a more oxygenated type II/III OM (Figure 7B).

After thermal maturations at 325−350 °C, a strong decrease in hopane, sterane, MAS, and TAS concentrations is observed (Figure 6). The content of alkanes, Phe, DBT, fluorenthenes, pyrenes, naphthalenes, and biphenyls increases. The concentrations reached by KCF samples after maturation at 350 °C are close to those of VK1 (Figure 5A). However, for similar
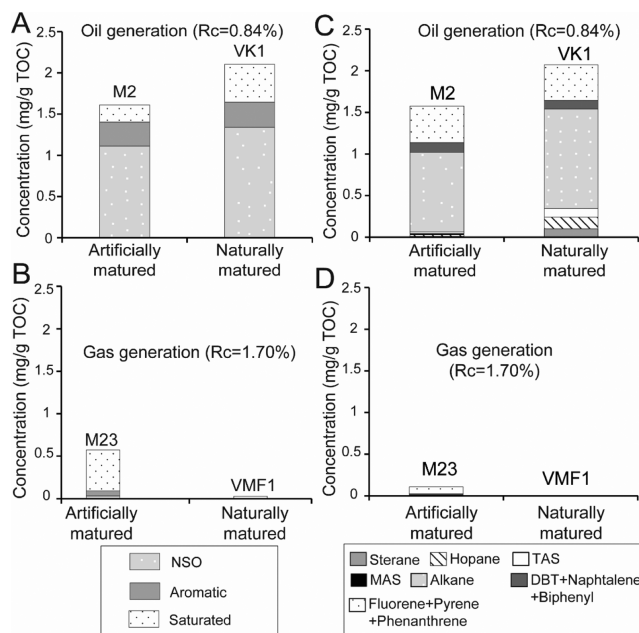
Figure 5. Comparison of (A,B) EOM concentrations, and (C,D) the detailed composition of the saturated and aromatic fractions between artificially matured KCF samples and naturally matured samples from the VMF and the Viking graben (VK1) during (A,C) oil generation and (B−D) gas generation. DBT: dibenzothiophenes. Alkane: n-alkanes, isoprenoids, alkylcycloalkanes. TAS: triaromatic steroids. MAS: monoaromatic steroids.

Rock Eval and thermal maturity parameters, VK1 contains slightly higher alkane concentrations than the artificially matured sample. Except the MAS, absent in VK1, similar components are present in VK1 and KCF samples (Figure 5A). As for the less oil-prone KCF samples, VK1 exhibits low Pr/n-C_{17}, Ph/n-C_{18} corresponding to a more oxygenated type II/III OM (Figure 7B).

After maturation a 350 °C, differences are observable between highly oil-prone and less oil-prone KCF rocks (Figure 6). Higher amounts of alkanes, DBT, and diaromatic HCs (naphthalenes and biphenyls) are present in highly oil-prone samples. Conversely, M2 and M23 show higher concentrations of fluorenthenes, pyrenes, and Phe. The concentration of Phe decreases while the concentrations of DBT and alkanes increase linearly with the initial content of orange AOM in the KCF series (Figure 4B,C). Normal-alkane concentrations (mainly C_{14}−C_{25}) increase after heating at 350 °C, but n-alkanes $< C_{14}$ are present in low amounts. At the same time, Ph/n-C_{18} and Pr/n-C_{17} decrease while Pr/Ph increases (Figure 7). Similar Pr/Ph is obtained in the naturally matured rock from the Viking graben (VK1) and from natural equivalents from the KCF and the Draupne fm. of previous studies.[59,60]
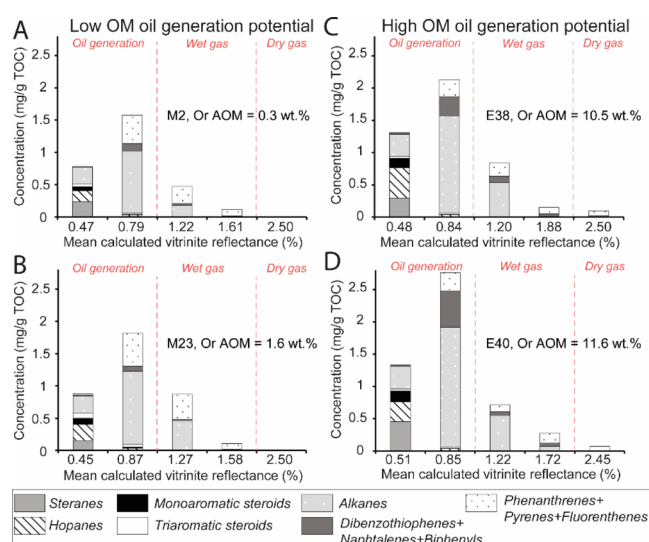
Figure 6. Concentrations of aromatic and saturated components of artificially matured Kimmeridge clay samples at different maturities of samples (A) M2, (B) M23, (C) E38, and (D) E40. Alkane: *n*-alkanes, isoprenoids, alkylcycloalkanes. Or AOM: orange AOM content (for the hopanes and steranes distributions, see the Supporting Information). The initial Or AOM increases from (A–D). Divisions of HC generation stages (dashed red lines) are based on R_c, Rock Eval parameters, and corresponding data form the literature.[29]
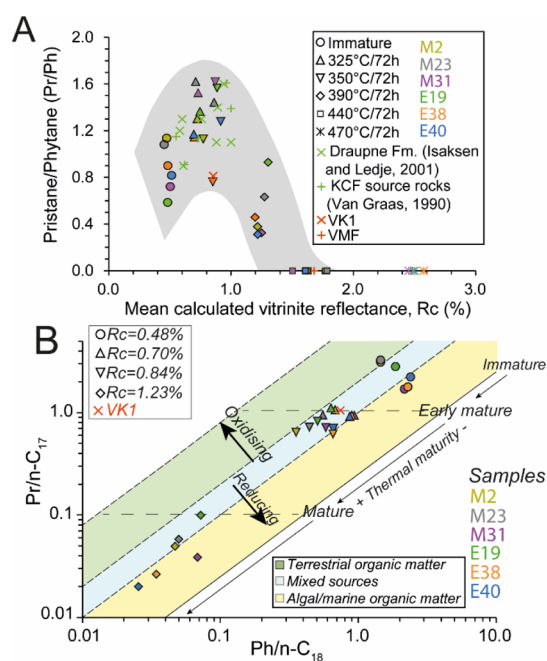
Figure 7. (A) Plot of pritsane/phytane vs the mean calculated vitrinite reflectance and (B) evolution of Pr/*n*-C17 versus Ph/*n*-C18 ratios (from Shanmugam[58]) for artificially matured KCF samples and naturally matured rocks from the Viking graben (VK1) and the Vaca Muerta fm. (VMF). (A) Comparison with pritsane/phytane of natural rocks from the Draupne (Isaksen and Ledje[59]) and the KCF (van Graas[60]). The highly oil-prone samples are M31, E38, and E40.

After maturation at 390, 440, and 470 °C, only Phe, fluorenthenes, pyrenes, and DBT are present in the EOM (Figure 6). Pr/Ph, Pr/*n*-C$_{17}$, and Ph/*n*-C$_{18}$ decrease (Figure 7). No residual organic components are present in VMF samples (Figure 5B,D).

Gas Composition. Small quantities of gas are generated after maturation at 325–350 °C (Figure 8A–D). CO_2 is the
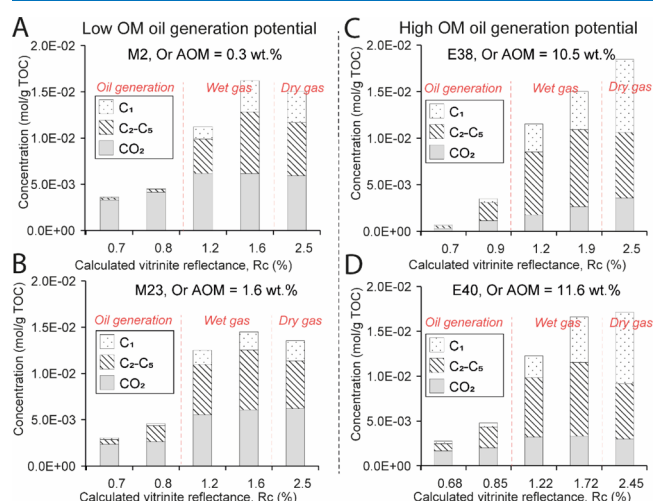
Figure 8. Variation in gas concentrations in samples (A) M2, (B) M23, (C) E38, and (D) E40 with increasing maturity. Or AOM: initial orange AOM content. Initial Or AOM increases from (A–D). Divisions of HC generation stages (dashed red lines) are based on R_c, Rock Eval parameters, and corresponding data from the literature.[29] We can see that the dry gas produced by our artificial maturation is lower than expected in the usual gas window.

most abundant (up to 4.14×10^{-3} mol/g TOC). The run at 390 °C is characterized by the strong increase in CO_2 and C_2–C_5 concentrations (Figure 8). Methane concentration is low after maturation at 390 °C ($\leq 3.0 \times 10^{-3}$ mol/g TOC) but increases progressively after heating at 440 °C and 470 °C (up to 7.95×10^{-3} mol/g TOC), while C_2–C_5 and CO_2 concentrations are relatively constant. C_2–C_5 concentration in the wet gas zone (Figure 9A), and C_1 in the dry gas zone (Figure 9B) increase linearly with the initial orange AOM content ($R^2 \geq 0.84$), while the amount of CO_2 decreases with increasing orange AOM content ($R^2 \geq 0.71$, Figure 9).

PSD and Pore Volume. The total pore volumes (V_{tot}) vary in KCF samples with increasing maturity (Table 1, Figure 10A). V_{tot} decreases after heating at 325 and 350 °C. This
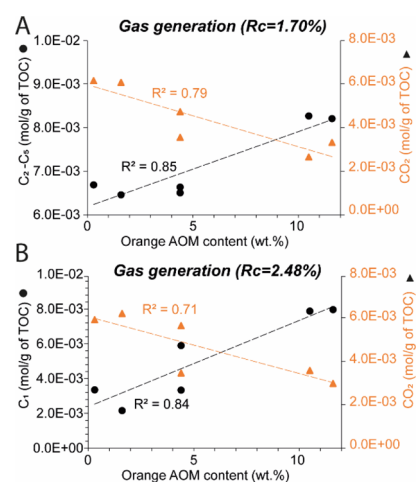
Figure 9. Evolution of (A) C_2–C_5 and (B) C_1 concentrations in Kimmeridge clay samples with increasing initial orange AOM initial content.
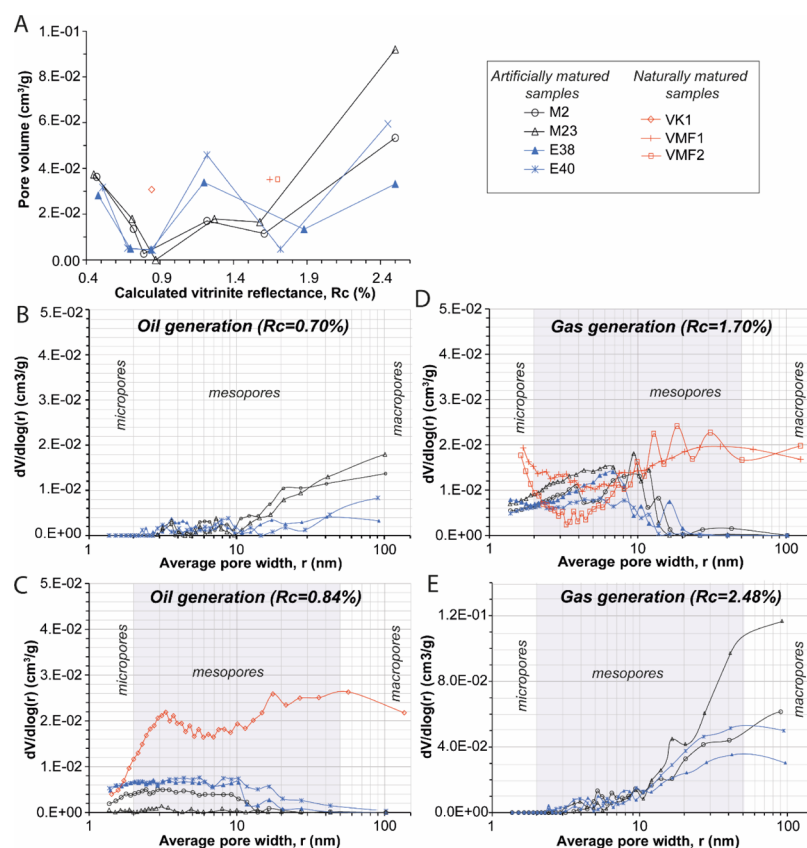
Figure 10. (A) Evolution of the pore volume of artificially matured KCF samples and natural rocks (red) from the Viking graben (VK1) and the Vaca Muerta (VMF). (B−E) BJH PSDs. Highly oil-prone samples are in blue. The legend is the same for (A−E). For readability reasons, the *y*-axis is not the same for (E).
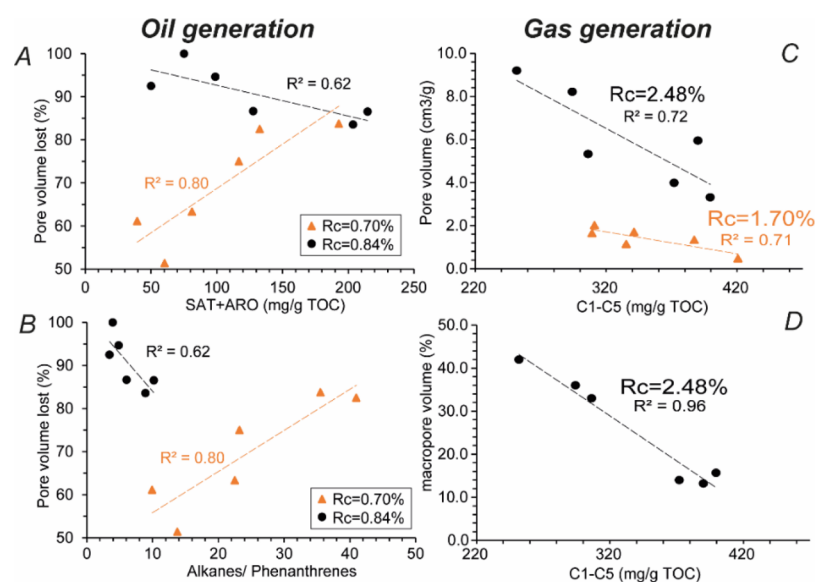
Figure 11. Percentage of pore volume lost in the oil generation stage as a function of (A) saturated + aromatic HCs (SAT + ARO), (B) alkanes/ Phe's ratio. (C) Evolution of pore volume as a function of the concentration of C_1−C_5 HC gases. (D) Evolution of the percentage of macropore volume as a function of the concentration of C_1−C_5 HC gases during gas generation.

corresponds to a decrease of the estimated porosity P accessible by nitrogen measurements from ≈6,0% (immature) to less than 1% (Table 1). After heating at 350 °C, samples are non-porous ($V_{tot} \leq 4.6 \times 10^{-3}$ cm³/g). M23 exhibits a very low $V_{tot} = 5.2 \times 10^{-4}$ cm³/g corresponding to a P < 0.1%. The residual pore volume is mainly composed of pores ≤20 nm

with ≈79% of mesopores (Table 1, Figure 10C). Most of the meso and macropores ranging from 10 to 100 nm in diameter, present after maturation at 325 °C (Figure 10B), are not visible after heating at 350 °C, but new meso and micropores varying from 1 to 10 nm in diameter are visible (Figure 10C). The percent of volume lost after heating at 325 °C in KCF
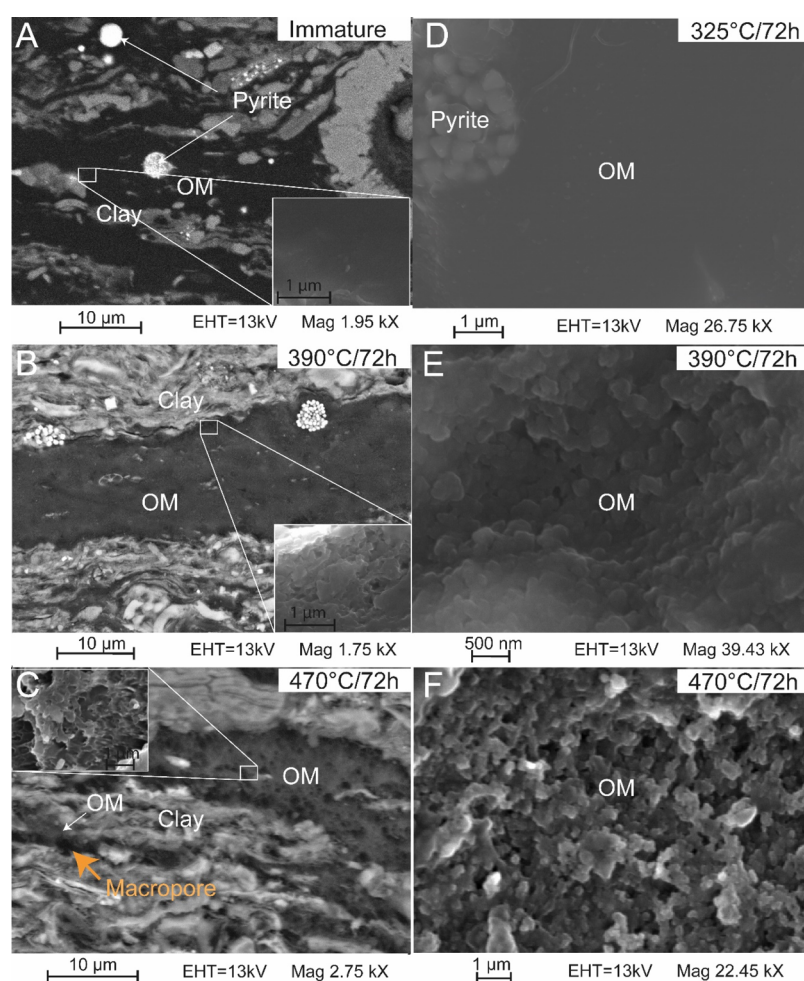
Figure 12. (A−C) SEM images in BSE mode of sample E40 (KCF) showing typical OM particles of KCF rocks (A) before thermal maturation and after maturation at (B) 390 and (C) 470 °C for 72 h. Insets in (A−C) are SE images showing the progressive evolution of the OM texture during maturation. (D−F) SEM images in SE mode showing the dominant texture of OM in sample E40 after maturation at (D) 325, (E) 390 and (F) 470 °C for 72 h. The OM texture evolved from a homogeneous smooth nonporous texture to a very porous granular texture with increasing maturity. The orange arrow in (C) shows a large macropore probably resulting from the important conversion of the OM particle during gas generation, leaving behind a large pore lined with residual OM.

rocks appears related to the concentration of SAT + ARO or to the alkanes/polyaromatic component ratio (such as Phe, Figure 11). This correlation disappears after maturation at 350 °C. After heating at 390 °C, V_{tot} increases (Table 1, Figure 10A). No correlation exists between pore volume, OM composition, and the concentration of C_1-C_5 generated at this maturity stage. The evolution of V_{tot} after maturation at 390−440 °C is then characterized by a succession of phases of reduction and growth of the pore volume (Table 1, Figure 10A).

After maturation at 440 °C for 72 h, samples exhibit low pore volumes (≤ 0.02 cm³/g), $\approx 83.8\%$ of which is accounted for by mesopores (Table 1).

The corresponding porosity P, which ranges between 3.2 and 8.6% after maturation at 390 °C, decreases to reach values ranging between 0.9 and 3.2% after heating at 470 °C (Table 1). Most of pores are smaller than 20 nm after maturation at 440 °C (Figure 10D). After maturation at 470 °C, V_{tot} exhibits a strong increase ($V_{tot} \geq 0.032$ cm³/g, Figure 10A). At this maturity stage, the measured V_{tot} corresponds to P ranging from 6.2 to 17.2%. Mesopores account for 58.0 to 84.7% of the pore volume (Table 1). While mesopores ranging between 2

and 10 nm in diameter are still present, most of the pore volume is composed of meso and macropores ≥ 10 nm in diameter (Figure 10E). The pore volume as well as the contribution of macropores decrease with increasing C_1-C_5 concentration (Figure 11C,D). VK1 exhibits a V_{tot} of 3.2×10^{-2} cm³/g ($P = 6.0\%$) composed of abundant macro and mesopores (Table 1, Figure 10C). VMF samples exhibit a V_{tot} of 0.035 cm³/g ($P = 6.5\%$) provided by abundant meso and macropores (Table 1, Figure 10D).

SEM Observations. SEM observations of KCF rocks before maturation show that, at the observation scale, the OM consists of large homogeneous non-porous particles (Figure 12A). After maturation at 325 and 350 °C (Figure 12D), no change is visible within the organic particles. The SEM does not allow a clear differentiation between the products generated by the OM thermal degradation and the initial OM material. No pores are visible in the OM at the observation scale (Figure 12D). After maturation at 390 °C, porosity formed in most of the organic particles giving them a slightly spongy texture in BSE images (Figure 12B). The pores appear essentially ≤ 200 nm in diameter. This OMp appears to be slightly more important after maturation at 470 °C (Figure
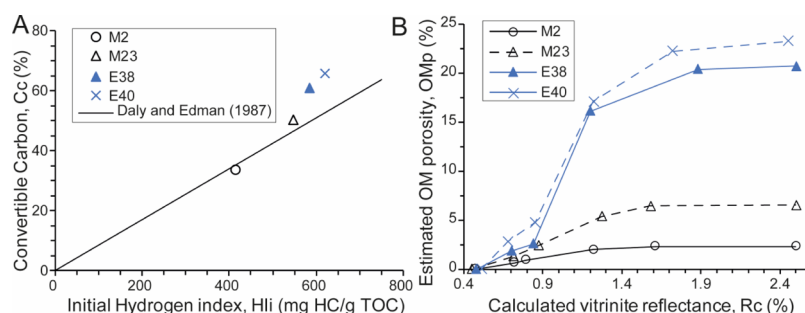
Figure 13. (A) Estimated convertible carbon content (after maturation at 470 °C) versus initial HI of artificially matured KCF samples. Comparison with trends from Orr:[61] Cc= 0.085 × HI$_i$. Cc (%) is the original organic carbon content of samples that can be converted into HCs during maturation. Each artificially matured sample come from a same original immature sample thermally matured at different temperatures. Cc is thus considered constant for each sample whatever their thermal maturities. (B) Variations of estimated OMp with increasing thermal maturity. Highly oil-prone samples are in blue.

12C). Pores are visible on a larger scale. Their diameter can be up to 500 nm. Larger pores lined with residual OM (2−4 μm in diameter) are also visible (orange arrow Figure 12C). SE images reveal that the appearance of pores in these OM particles is tied with a drastic change of the OM texture (Figure 12D−F). Before maturation, the OM exhibits a smooth homogeneous texture (Figure 12D) which become more and more granular with increasing maturity. After heating at 390 °C, the OM appears mainly as slightly granular particles hosted small size pores (generally less than 200 nm, Figure 12E). After maturation at 470 °C, OM consists in very granular particles formed of the aggregation of small spherical structures separated by larger pores up to 500 nm in diameter (Figure 12F).

Estimated OMp. Cc values of artificially matured KCF rocks vary between 34 and 66% after maturation at 470 °C and increase with the initial HI to follow the general trend observed by Orr[61] for a type II kerogen (Table 1, Figure 13A). After maturation at 390 °C, the calculated OMp increases strongly to reach values ranging from 2.0 (less oil-prone rock) to 17.1% (highly oil-prone rock). After heating at 440−470 °C, OMp continues to increase but slowly to reach values varying between 2.3% for the less oil-prone rock to 23.3% for the highly oil-prone. The OMp of the highly oil-prone sample (E38 and E40) is about 10 times more important than the OMp of the less oil-prone samples (M23 and M2, Figure 13B).For R_c > 1.30%, the calculated TR is >85% (Table 1), while for R_c <0.90%, the calculated TR is <40%.

■ DISCUSSION

OM Composition. KCF rocks are known to contain a type II oil-prone AOM derived mainly from resistant cell walls of microalgae (brown AOM) and oil-prone phytoplanktonic lipidic components preserved by natural sulfurization (orange AOM). This is well substantiated by our molecular analyses which show the presence of abundant mid molecular weight *n*-alkanes (C$_{21}$−C$_{25}$) known to be derived mainly from freshwater aquatic and marine macrophytes.[62,63] Our results show differences in OM composition between samples. Orange AOM-poor samples contain a greater proportion of more oxygenated type II/III OM (Figure 7B). These samples correspond to non-productive periods that were less favorable to the production and the preservation of the oil-prone phytoplanktonic material. Orange AOM-rich samples probably formed during periods of higher phytoplanktonic productivity, allowing a better preservation and exportation of this oil-prone

material. This is well substantiated by the plot of Pr/*n*-C$_{17}$ versus Ph/*n*-C$_{18}$ which shows the presence of less oxygenated type II OM formed in reducing conditions (Figure 7B). Preserved by sulfurization processes,[42] the higher proportion of orange AOM explains the higher DBT, hopane, and sterane contents of oil-prone rocks[64] (Figure 6).

Thermal Maturity and OM Transformations during Maturation. The R_m and the R_c <0.50% and the values of Pr/*n*-C$_{17}$ and Ph/*n*-C$_{18}$ before maturation corroborate the immaturity of KCF samples (Table 1, Figure 7A). Gas, EOM composition, and R_c are well substantiated by the R_m of 0.66, 1.40, and 2.02% measured after maturation at 325, 390, and 470 °C respectively (Table 1, Figures 2 and 8). This indicates the progressive increase in the thermal maturity from the early oil window to the dry gas zone. The R_c of ≈0.85%, the strong increase in EOM, SAT, and ARO concentrations, and the increase in the amount of di-, poly-aromatic HC, and *n*-alkanes indicate that the peak of oil generation was reached after maturation at 350 °C (Figures 2 and 6). The comparison of the relative proportion of SAT, ARO, and NSO of our artificially oil-matured samples with the mean of 636 natural crude oils from Tissot and Welte[25] shows that the content of SAT and ARO are low after artificial thermal maturation (Figure 3). This observation may suggest that oil migration leads to the segregation of the heaviest NSO compounds, causing the natural enrichment of crude oils in SAT and ARO compared to our total EOM from artificial maturation experiments. This well substantiates the work of Jubb et al.[65] which showed a loss of carbonyl groups and a decrease of the length of alkyl chains as migration distance increase in unconventional petroleum source bed of the Ordovician Stonewall Formation. However, the EOM of the natural oil-mature sample (VK1) exhibits also slightly higher concentrations of SAT and alkanes than the artificially matured rocks (Figure 5A,C). We suggest that the short duration and the high temperatures of our artificial maturations may lead to the production of lower amounts of SAT compared to natural systems. After maturation at 325 and 350 °C, the strong decrease in sterane and hopane concentrations marks the progressive degradation of the less thermally stable components (Figure 6). Pr/Ph increases in the same time to reach similar values of natural mature source rocks from the KCF or equivalent formations of the North Sea (Draupne fm.),[52,53] confirming that these thermal maturation experiments have accurately simulated the OM thermal transformation (Figure 7A). The thermal cracking of OM after heating at 350 °C

results in the generation of $C_{14}-C_{25}$ *n*-alkanes (Figure 6). Only ≈27 and ≈8% of the total concentration of C_2-C_5 and C_1 have been generated during the peak of oil generation, respectively (Figure 10). These results well substantiate the work by Behar et al.[27] which showed that the thermal cracking of a type II OM first results in the production of alkanes > C_{14} and in the production of ~30 wt % of the C_2-C_5 but only 5 wt % of the methane fraction.

The evolution of gas concentrations and the R_c indicate that the beginning, the middle, and the end of the gas generation zone have been reached after maturation at 390, 440, and 470 °C respectively (Table 1, Figure 8). The R_m of 1.40 and 2.02% measured after maturation at 390 and 470 °C are consistent with these results (Table 1). However, the still very high concentrations of C_2-C_5 compared to C_1 in the dry gas zone are surprising (Figure 8). Thus, while biomarkers, calculated, and measured vitrinite reflectance values indicate that the dry gas window has been reached, it would appear that under these thermal maturation conditions and based on gas concentrations alone, the production of gas seems to be similar to the one produced near the end of the usual wet gas window. We can suggest that the short thermal maturation duration may have limited or delayed the conversion of C_2-C_5 HC to methane leading to a discrepancy between the predicted maturity, the thermal maturity indicated by the evolution of biomarkers and the real OM thermal maturity for the highest stage of maturation. It is quite normal to think that the HC produced by short-term artificial thermal maturations at high temperatures is somewhat different from long-time geologic maturations at lower temperatures. However, according to the available literature,[31,66,67] the evolution of Pr/Ph, Pr/*n*-C_{17}, and Ph/*n*-C_{18} substantiates the degrees of maturity for the lower maturity stages (Figure 7). The R_c thus provides a relatively good estimate of the vitrinite reflectance, especially from the low mature stage to the beginning of wet gas generation (Table 1). However, beyond, the R_c varies greatly between samples and seems to overestimate the maturity. If the calibrations curves and the equations made between the MPI-1, the DPR, the MDR, and the vitrinite reflectance reported by Boreham et al.[28] Radke,[32] and Radke et al.[51] are very accurate for maturities ranging from 0.50 to 1.70%, they lose in accuracy beyond 1.70% because of the lower number of gas-mature samples used. The precision of the R_c calculated using these ratios is therefore decreasing for R_c > 1.70%. This may explain the slightly higher variability of our R_c values after maturation at 440 and 470 °C. These ratios need thus to be compared with other parameters to ensure a reliable estimate of thermal maturity. Wet and dry gas generation is marked by the progressive thermal degradation of SAT and ARO (Figure 2). Alkanes, di-, and heavier polyaromatic HC are progressively converted into C_1-C_5 components (Figures 6 and 8). After maturation at 390 to 470 °C, the secondary cracking of OM left behind a residual inert OM with no remaining HC potential (HI < 30 mg HC/g TOC, Table 1). While about 64% of the *n*-alkanes generated during maturation are degraded during the early condensate wet gas zone to generate C_2-C_5, only ~48% of the methane is produced (Figures 6 and 8). At this maturity stage, *n*-alkanes <C_{14} are still present in low amounts suggesting that even if these components are generated during OM thermal degradation, they are probably quickly degraded into C_2-C_5. Methane appears to be mainly produced from the end of the wet gas zone to the dry gas zone, when all the alkanes have been degraded and the C_2-C_5

concentrations start to decrease (Figure 8). These results substantiate previous works[27] and suggest that methane is mainly produced from the thermal degradation of the C_2-C_5 fraction.

The OM molecular analyses show that the concentration and the geochemical composition of EOM and gas generated during maturation closely depend on the initial proportion of orange AOM (Figures 4 and 9). The thermal cracking of samples richer in orange AOM generated more abundant less viscous oils enriched in SAT during oil generation. These samples are characterized by lower amounts of NSO, higher proportions of ARO and SAT richer in *n*-alkanes, and light aromatic HC (biphenyls, naphthalenes, DBT, Figures 4 and 6). The secondary cracking of this more hydrogenated OM then resulted in the formation of larger amounts of C_1-C_5 gases (Figure 8C,D). On the contrary, the thermal degradation of the orange AOM-poor samples and the apparent heavier and less abundant viscous oils produced from them led to the formation of smaller quantities of C_1-C_5 and more abundant CO_2 (Figures 8A,B and 9).

Thermal Maturity and OM Geochemical Composition as Controlling Factors of KCF Mudstones Porosity. Gas generation generally coincides with the massive development of pores within sedimentary OM and pyrobitumen in response to the massive production and expulsion of gaseous HC.[2,5,6,10,12,21,34,68−70] This is well substantiated by the evolution of the OMp of artificially matured KCF rocks calculated using the equation reported by Modica and Lapierre[8] (Figure 13B). Depending on the measured rock Eval parameters, these results show, indeed, a very strong increase in the OMp, especially during the early wet gas generation, where the increase of the TR is the most important (Table 1). The evolution of TR after thermal maturation follows the trend generally observed for a type II OM.[8,52,71,72] Cc values correspond also to the Cc data obtained for a type II OM.[8,61,71] This shows the general representativeness of the results obtained from our laboratory experiments and confirms that the OMp is supposed to increase progressively with increasing maturity and gas generation up to reached ~23% in the highly oil-prone samples (Figure 13B). This increase in the OMp is well supported by SEM observations, which show the appearance of pores within the organic particles from the beginning of the gas window (R_m = 1.40%, 390 °C/72 h, Figure 12B). As for the calculated OMp (Figure 13B), the observed OMp has slightly increased at the higher maturity stages, especially in terms of pore size because pores up to 500 nm in diameter are clearly visible in SEM after maturation at 470 °C (Figure 12C,F), while pores after heating at 390 °C are mainly less than 200 nm in diameter (Figure 12B,E). SEM SE images reveals that the formation of pores in OM is accompanied by a significant and progressive change of the OM texture from a smooth homogenous texture (before maturation up to the oil generation) to a very heterogeneous granular texture formed from the aggregation of small spheres (with sizes ranging from 250 to 500 nm in diameter) of OM after maturation at 470 °C (Figure 12D−F).

After maturation at 350 °C, nitrogen adsorption data show that OM is mainly micro and mesoporous (<10 nm, Figure 10C). Most of the mesopores and macropores ≥10 nm in diameter previously observed after maturation at 325 °C (Figure 10B) where they are thus probably filled by oil at this maturity stage, explaining the loss of pore volume (Figure 10A). However, the formation of new pores less than 10 nm is

observed after heating at 350 °C (Figure 10C). This could be explained by the formation of supplementary pores in the OM as indicated by the slight increase of the OMp (Figure 13A) or by the reduction of size of macro and mesopores because of their partial filling by oil. The OMp often appears to be equal or significantly higher than the porosity P of the rock accessible to nitrogen determined from the V_{tot}. For example, in the oil window, the P varies from 0.1 to 3.4%, while the OM ranges between 0.6 and 4.8%. Note that only pores between 0.6 and 200 μm in diameter that are sufficiently connected to each other are accessible to the nitrogen during adsorption measurements and therefore counted in the pore volume and P. The pore volume represented by the OMp is not necessarily accessible to nitrogen. The throats of these pores or other pores through which they are connected may be too small for nitrogen molecules. Moreover, many of the pores associated with the mineral matrix and the OM are, at this maturity stage, probably weakly connected or partially filled by oils and are therefore inaccessible to nitrogen. This can prevent the passage of nitrogen and avoid the detection of these pores by gas adsorption techniques. Thus, even if this OMp is present, it is not necessarily an effective and measurable porosity. At least half of the OMp seems thus not accessible to the gas in the oil window. This is probably the reason why M23 exhibits a so very low $V_{tot} = 5.2 \times 10^{-4}$ cm^3 g after maturation at 350 °C. Nitrogen probably did not succeed to access enough pores in M23. This shows that a large part of the pore volume and the total porosity of the rock are not taken into account in nitrogen adsorption data. This OMp calculated during the oil generation stage is not observed in SEM SE images (Figure 12D) probably filled by oil or too small to be observed at the SEM observation scale. The same applies to the gas window, where the OMp reaches up to 23.3% for E40 while P does not exceed 11.2%. In view of these results, it is clear that V_{tot} and P are significantly underestimated. However, this underlines the importance of the contribution of the OMp to the porosity and gas storage capacities of the studied samples.

In view of the continuous increase of the OMp, we thus expected a continuous increase in nitrogen adsorption rock pore volume during maturation. This is not the case. The decrease in measured pore volumes and global pore size after thermal maturation at 440 °C ($R_c \approx 1.70\%$) and their re-increase after maturation at 470 °C indicate that the secondary cracking of OM does not lead to a continuous and linear increase of P, the porosity accessible to gas in samples (Figure 10A). After maturation at 440 °C, HC generation may have deformed the OM structure leading to the decrease of the pore volume at the end of the condensate/wet gas zone ($R_c = 1.70\%$). While the OMp continues to increase slowly at higher maturity stages (Figures 12 and 13B), these modifications may have resulted in a temporary loss of connectivity of samples' pore network, considerably reducing the accessibility of pores to nitrogen during nitrogen adsorption analyses. However, this indicates that the porosity of mudstones accessible to gas is not systematically preserved in its entirety during gas generation. These variations of the pore network and the ensuing loss of the pore volume during nitrogen adsorption measurements seem to be influenced by the amount of HC gases generated during maturation and thus on the initial OM composition. For the two higher maturity stages, the concentration of gaseous HC seems, indeed, to be correlated with KCF porosity and macropore volume (Figure 11C,D). The more C$_1$–C$_5$ HC gases the samples have generated, the more the resulting interconnected pore network may have suffered alteration of the pore volume, leading to a loss of pore interconnectivity and thus of the macropore volume accessible to nitrogen (Figure 11D). V_{tot} and especially the volume of macropores of the studied samples decrease with the amount of C$_1$–C$_5$ HC gases and thus with the initial content of oil-prone orange AOM (Figure 11). For Cavelan et al.,[21] this difference of porosity between KCF samples is due to a different ability of rocks to form and to preserve pores during gas generation. For them, this ability may be directly inherited from the initial shape and distribution of the different macerals present in rocks. Our results indicate, however, that this difference may not only be related to the initial structure of the macerals present in samples, more or less resistant to compaction, but also to the different initial molecular composition and oil and gas generation potential of these particles during maturation. During oil generation, the percentage of volume lost in KCF samples seems correlated with the concentration of SAT and ARO and the relative proportion of light/heavy HC (alkanes/Phes) generated during maturation (Figure 11A,B). The relative proportion of light and heavy HC and the ensuing viscosity of EOM may have influenced the ability of EOM to impregnate the mineral matrix during oil generation. For similar TOC and thermal maturity, orange AOM-poor rocks generated lower concentrations of heavier EOM enriched in NSO and polyaromatic components (Figure 4). In limiting the ability of oil to impregnate and fill the mineral-associated porosity, this variation of EOM composition may have led to the preservation of a greater part of the mineral-associated porosity in the less oil-prone rocks. This may explain a small part of the greater pore volume of these samples during gas generation (Table 1). On the contrary, highly oil-prone rocks (orange AOM-rich samples) which have generated higher amounts of saturated and aromatic HC, richer in hydrogenated and lighter components, such as n- and isoalkanes (Figure 4), exhibited a greater loss of pore volume during oil generation (Table 1, Figure 10), more efficiently filled by EOM, limiting the interconnectivity of pores and the contribution of the mineral-associated pore network to the total porosity. In changing the viscosity and the distribution of EOM in the mineral matrix, this phenomenon may also influence the distribution of pores known to partly form within residual OM (pyrobitumen) during the secondary cracking of OM[2,6,21,68,69] and their ability to resist to deformations. For example, Wood et al.[26] suggested that variations of the initial composition of pyrobitumen can be at the origin of the variations of porosity and texture observed in pyrobitumen particles in the Montney Fm. As previously discussed, the remaining pore volume associated with the mineral matrix and, in a less extant to the OM (OMp < 5%, Figure 13B), is probably too weakly connected to the peak of oil generation (350 °C/72 h) to be correctly measured by nitrogen adsorption. These correlations are thus no longer visible at this maturity stage (Figure 11). Small variations in the initial OM composition and its ability to generate oil and gas seem therefore to affect the pore volume of mudstones during maturation. These variations have nevertheless a much less consequential impact than the effect of thermal maturity, which remains the major process controlling the evolution of porosity. These processes need to be considered in the case of samples with a relatively heterogeneous OM composition but could probably be neglected in other cases.

After maturation at 440 and 470 °C, the V_{micro} and the V_{meso} decrease while the V_{macro} and the V_{tot} increase (Table 1). This can be explained by two phenomena: (i) the progressive coalescence of certain meso and micropores formed earlier during maturation. Thus, part of the micropores and the mesopores, still present after maturation at 470 °C (Figure 10E), join to form larger hybrid meso and macropores ≥20 nm in diameter. As observed in the Figure 10D, this hybrid macro and mesopores become thus the largest contributor to the V_{tot}. SEM images (Figure 12E,F) suggest that the change of the OM structure to this aggregation of small residual spheres of OM is tied with this pore coalescence; (ii) the important conversion of some organic particles forms very large macropores lined with residual OM, already documented in previous studies.[14,22] These pores correspond to spaces formerly occupied by OM which has been converted into oil and gas during maturation. Even if they are not predominant, the very large size of these pores (up to several micrometers in diameter in SEM) largely contributes to the V_{tot} and thus to the % of volume occupied by macropores (V_{macro}). That greatly reduces the proportion of the volume occupied by meso and micropores and can explain the observed data.

Representativeness of Artificial Thermal Maturation Experiments. Artificially matured KCF rocks and the natural oil-mature sample (Viking graben, VK1) show similar OM composition and biomarker ratios (Figures 5 and 7B). This well corroborates the similar origin of their OM. However, for the same thermal maturity and OM content, artificially matured samples contain lower concentration of SAT, alkanes (n-alkanes, hopanes, and steranes), and a slightly lower amount of polyaromatic components (Figure 5). This may suppose that the shorter duration of maturation experiments and the higher temperatures can lead to a less efficient conversion of the OM into bitumen enriched in SAT. Previous works showed indeed that increasing the duration of artificial maturation experiments and the residence time in the system may enhance the degradation of heavy NSO OM components into lighter components.[29,73] The high temperature used during maturation experiments has probably led to a faster thermal degradation of hopanes and steranes. This may explain the higher residual hopane and sterane contents of the natural oil-prone sample (VK1) compared to the artificially matured rocks. Furthermore, VK1 exhibits a higher pore volume than artificially matured samples during oil generation (Figure 10A). This higher pore volume is provided by a greater meso and macroporosity (Figure 11B). The PDS of VK1 is similar to those previously observed by Cavelan et al.[43] in immature KCF rocks. Contrary to our artificially matured samples, we can suggest that a part of the EOM generated by VK1 has probably migrated, partly releasing the porosity of the mineral matrix. The amount of EOM initially produced by VK1 was thus probably greater. The VMF contains initially the same type II KCF-like OM precursor dominated by marine algal AOM.[46,47] However, for similar maturities, artificially matured KCF samples contain higher residual EOM concentrations than VMF rocks (Figure 5). The shorter duration used for thermal maturation experiments seems to have limited the thermal degradation of OM leading to higher residual EOM contents and probably to different C_1–C_5 concentrations. This probably explains the very low methane concentration after maturation at 470 °C, while the values of R_c and R_m indicate that the dry gas window must have been reached (Figure 8). Despite a similar OM precursor, the slightly different mineralogy of VMF

mudstones (≈26 wt % of clay contents)[43] and the difference of OM thermal degradation kinetics may be at the origin of the difference of porosity observed between VMF and artificially matured KCF rocks during gas generation (Table 1, Figure 10A,E). Hence, for the same thermal maturity, VMF rocks exhibit a higher pore volume and, especially, a greater meso and macroporosity than KCF mudstones. This probably reflects a different ability of the rock framework to preserve pores tied with a different mineralogical composition. Moreover, it is important to consider that the high temperature of our confined experiments may enhanced both the ductility of the rock with increasing maturity and the deposition of coke because of enhance OM thermal degradation processes. This may lead to different ability of the rock to form and preserve pores between natural and laboratory conditions. This comparison highlights the usefulness of comparing natural and artificially matured samples in order to put aside the limitations existing in these artificial maturation systems.

Significant differences of porosity and OM composition exist between experimental and natural oil and gas-mature samples. In view of the more frequent use of artificial maturation experiments to assess organic-rich mudstones porosity these last years,[4,10,74,75] it could be interesting to compare these results with longer duration laboratory experiments to better understand the influence of the maturation kinetics on the simulated OM thermal degradation processes and pore development. Moreover, the water present in natural reservoirs is generally considered to be the main source of hydrogen involved for OM thermal degradation.[35] Lewan[35,76] demonstrated that without water, the cross-linking of C–C bonds is favored rather than the breaking of C–C bonds during maturation. This favors the formation of carbon-rich residue that may significantly prevent or limit the generation of SAT-rich oil during maturation. The anhydrous conditions of our thermal maturations may thus have partially contributed to the differences in SAT contents and porosity observed between naturally and artificially matured samples. However, if water was not added in excess in gold cells during the experiments, gas analyses show that water has been naturally generated during our laboratory simulations (not presented). According to previous works,[21,77,78] we suppose that the presence of this water generated from OM conversion and clay-minerals transformation has limited the effects of water on OM thermal degradation and porosity development during maturation. Nevertheless, these different conditions of pyrolysis may partly explain differences in PSD observed during gas generation between our work and data from the literature. For example, reports of Wang et al.[34] show that the hydrous pyrolysis of shales from the Mesoproterozoic Xiamaling Formation results mainly in the increase of the microporosity (<2 nm) in diameter during gas generation while the meso- and the macroporosity decrease. We observed the contrary. Landais et al.[29] showed that under the high temperature of artificial maturations, the ability of water to enter the OMp is altered. As a result, hydrous conditions may delay the conversion of the OM.[29] In the case where most of pores result from the conversion of the OM, we can suggest that the delay of HC and gas generation under hydrous conversion may explain that only micropores were formed during gas generation for Wang et al.,[34] while these micropores have already coalesced to form larger meso and macropores in our study under anhydrous conditions. Pyrolysis conditions may thus have a significant impact on porosity development. This also means that direct

comparisons of results of different works remain only possible between maturities carried out under similar conditions and on samples of the same organic and mineralogical characters. It is also important to mention that our experiments carried out on powder and under a hydrostatic confining pressure do not permit the reproduction of the lithostatic pressure present in natural environments. Indeed, during our laboratory simulations, natural lithostatic pressure, which can affect the structure of the organic solids at high maturity stages (preferential orientation of condensed aromatic sheets in residual OM[56,79]) is replaced by an external hydrostatic pressure applied on the gold cell during the confined thermal maturation. Hence, in our experiments, the pressure is only transmitted by the effluents generated during the maturation (small amounts of water in vapor state, HC and gases). While this factor ensures the confinement (minimum dead volume) required for the simulation of OM thermal degradation,[30,79] this device cannot accurately reproduce the relations between oil expulsion, retention processes, and porosity that exist in natural systems under lithostatic pressure. This study shows that the production of saturated, aromatic, HC gases, and their relative proportions have an influence on porosity. The extent of the influence of this phenomenon varies probably in natural systems, where the kinetics of maturation is different and where the lithostatic pressure has a considerable impact on the intra and intergranular porosity. This means that the role of these processes is probably weaker because of the competition from other phenomena that may occur in natural systems. Nevertheless, the number of natural samples used for comparison in our study is too small to go any further in this approach.

SUMMARY AND CONCLUSIONS

Kimmeridge clay mudstones with different type II OM oil-generation potential were artificially matured to simulate the OM thermal degradation and the subsequent variations of OM molecular composition and pore volume. These results were compared with natural oil-mature and gas-mature rocks from the Viking graben (Kimmeridge Clay fm.) and the Vaca Muerta fm., respectively. The following conclusions can be drawn.

The variations of the OM oil-generation potential caused differences in the amount and the geochemical composition of the products generated during maturation. The increase of the initial content of the phytoplanktonic OM leads to (i) the increase of the concentration of saturated (mainly $C_{14}-C_{25}$ n-alkanes) and diaromatic HCs (DBTs, asphaltenes, and biphenyls) generated during oil generation; (ii) the increase of C_2-C_5 HCs produced in the condensate wet gas zone and to the decrease of the amount of CO_2; and (iii) the increase of methane generated mainly during the dry gas zone. During oil generation, the relative proportion of light and heavier HC generated seems to affect the ability of EOM to fill the adjacent pores of the mineral matrix and thus the ability of the rock to preserve its initial porosity. For similar TOC, highly oil-prone rocks generated higher amounts of saturated-rich EOM and exhibited lower pore volumes.

In accordance with SEM observations the calculated OMp increases during maturation, especially from the condensate wet gas zone, in response to the OM conversion. However, the secondary cracking of OM does not lead to a continuous increase of the rock pore volume. A significant loss of pore volume occurs at around $R_m \approx 1.40\%$. The intensity of this

phenomenon seems linked to the amount of HC gases generated and thus on the initial OM oil-prone quality. The more C_1-C_5 HC gases the samples have generated, the more the sample pore network seems to have suffered severe pore volume alterations, leading to a loss of pore volume. Hence, contrary to what is currently accepted in the literature, the ability of KCF source rocks to develop pores can decrease with the initial OM oil-generation potential. These variations have nevertheless a smaller impact than the effect of thermal maturity, which remains the major process controlling the evolution of porosity.

Differences in the concentrations of saturated and aromatic components as well as significant differences in pore volume and PSD exist between naturally and artificially matured samples. The time allowed for the OM thermal degradation processes seems thus to impact the thermal transformations of OM and the porosity. The very high concentrations of C_2-C_5 compared to C_1 generated in the dry gas zone suggest also that the very short thermal maturation duration may have limited or delayed the conversion of C_2-C_5 HCs to methane. Hence, a discrepancy exists between the thermal maturity indicated by the vitrinite reflectance and gas composition for the higher stage of maturity. For a better understanding, additional investigations on the role of the artificial maturation kinetics on oil generation and porosity are required.

APPENDIX

Calculation of TR, Cc, and biomarker ratios

- MDBT: methyldibenzothiophene ratio = 4-MDBT/1-MDBT.[32]
- MDR R_c % = 0.40 + 0.30 × MDR − 0.094 × MDR^2 + 0.011 × MDR^3.[32]
- DPR: dimethylphenanthrene ratio = (2,6-DMP + 2,7-DMP + 3,5-DMP)/(1,3-DMP + 1,6-DMP + 2,5-DMP + 2,9-DMP + 2,10-DMP + 3,9-DMP + 3,10-DMP).[32]
- DPR R_c % = 1.50 + 1.34 × $\log_{10}$ DPR.[32]
- MPI-1: methylphenanthrene index = 1.5 × (2-MP + 3MP)/(Ph + 1-MP + 9-MP).[51]
- MPI-1 R_c %: for $R_o \leq 1.4\%$, R_o = 0.7 × MPI-1 + 0.22.[28]

For $R_o \geq 1.4\%$, R_c = −0.55 × MPI-1 + 3.0.[28]

- Mean R_c = (MDR R_c %+ DPR R_c %+ MPI-1 R_c %)/3.
- Transformation ratio (TR) = $(S_{2i} - S_{2m})/(S_{2i})$;[52] with S_{2i}, the S_2 of the immature sample, and S_{2m} the S_2 of the same sample after thermal maturation.
- Convertible carbon (Cc) = (1/TR) × (1 − [TOC_m/TOC_i])[52] with TOC_i the TOC of the immature sample and TOC_m the TOC of the same sample after thermal maturation.

ASSOCIATED CONTENT

ⓈI Supporting Information

The Supporting Information is available free of charge at https://pubs.acs.org/doi/10.1021/acsomega.0c01432.

Full description of GC-TCD, GC−MS, SEM, and Rock Eval methods; n-alkanes, hopanes, steranes, monoaromatic, and TAS distribution; Rock Eval 6 S_2; and main biomarker ratios: MDBT, MPI-1, DPR, 20S/(20S + R), 22S/(22S + R), Pr/n-C17, and Ph/n-C18, Pr/Ph (PDF)

■ AUTHOR INFORMATION

Corresponding Author
Mohammed Boussafir − *Université d'Orléans, ISTO, CNRS UMR 7327, 45100 Orleans, France;* ● orcid.org/0000-0001-6081-6456; Phone: +33 2 38 49 72 26; Email: mohammed.boussafir@univ-orleans.fr

Authors
Amélie Cavelan − *Université d'Orléans, ISTO, CNRS UMR 7327, 45100 Orleans, France*
Claude Le Milbeau − *Université d'Orléans, ISTO, CNRS UMR 7327, 45100 Orleans, France*
Fatima Laggoun-Défarge − *Université d'Orléans, ISTO, CNRS UMR 7327, 45100 Orleans, France*

Complete contact information is available at:
https://pubs.acs.org/10.1021/acsomega.0c01432

■ REFERENCES

(1) Bernard, S.; Horsfield, B.; Schulz, H.-M.; Wirth, R.; Schreiber, A.; Sherwood, N. Geochemical Evolution of Organic-Rich Shales with Increasing Maturity: A STXM and TEM Study of the Posidonia Shale (Lower Toarcian, Northern Germany). *Mar. Pet. Geol.* 2012, 31, 70−89.

(2) Bernard, S.; Wirth, R.; Schreiber, A.; Schulz, H.-M.; Horsfield, B. Formation of Nanoporous Pyrobitumen Residues during Maturation of the Barnett Shale (Fort Worth Basin). *Int. J. Coal Geol.* 2012, 103, 3−11.

(3) Chalmers, G. R. L.; Bustin, R. M. Lower Cretaceous Gas Shales in Northeastern British Columbia, Part I: Geological Controls on Methane Sorption Capacity. *Bull. Can. Pet. Geol.* 2008, 56, 1−21.

(4) Chen, J.; Xiao, X. Evolution of Nanoporosity in Organic-Rich Shales during Thermal Maturation. *Fuel* 2014, 129, 173−181.

(5) Curtis, M. E.; Cardott, B. J.; Sondergeld, C. H.; Rai, C. S. Development of Organic Porosity in the Woodford Shale with Increasing Thermal Maturity. *Int. J. Coal Geol.* 2012, 103, 26−31.

(6) Loucks, R. G.; Reed, R. M.; Ruppel, S. C.; Jarvie, D. M. Morphology, Genesis, and Distribution of Nanometer-Scale Pores in Siliceous Mudstones of the Mississippian Barnett Shale. *J. Sediment. Res.* 2009, 79, 848−861.

(7) Yang, S.; Chen, G.; Lv, C.; Li, C.; Yin, N.; Yang, F.; Xue, L. Evolution of Nanopore Structure in Lacustrine Organic-Rich Shales during Thermal Maturation from Hydrous Pyrolysis, Minhe Basin, Northwest China. *Energy Explor. Exploit.* 2018, 36, 265−281.

(8) Modica, C. J.; Lapierre, S. G. Estimation of Kerogen Porosity in Source Rocks as a Function of Thermal Transformation: Example from the Mowry Shale in the Powder River Basin of Wyoming. *AAPG Bull.* 2012, 96, 87−108.

(9) Han, Y.; Horsfield, B.; Wirth, R.; Mahlstedt, N.; Bernard, S. Oil Retention and Porosity Evolution in Organic-Rich Shales. *AAPG Bull.* 2017, 101, 807−827.

(10) Ko, L. T.; Ruppel, S. C.; Loucks, R. G.; Hackley, P. C.; Zhang, T.; Shao, D. Pore-Types and Pore-Network Evolution in Upper Devonian-Lower Mississippian Woodford and Mississippian Barnett Mudstones: Insights from Laboratory Thermal Maturation and Organic Petrology. *Int. J. Coal Geol.* 2018, 190, 3−28.

(11) Ko, L. T.; Loucks, R. G.; Zhang, T.; Ruppel, S. C.; Shao, D. Pore and Pore Network Evolution of Upper Cretaceous Boquillas (Eagle Ford−Equivalent) Mudrocks: Results from Gold Tube Pyrolysis Experiments. *AAPG Bull.* 2016, 100, 1693−1722.

(12) Reed, R. M.; Loucks, R. G.; Ruppel, S. C. Comment on "Formation of Nanoporous Pyrobitumen Residues during Maturation of the Barnett Shale (Fort Worth Basin)" by Bernard et al. (2012). *Int. J. Coal Geol.* 2014, 127, 111−113.

(13) Fishman, N. S.; Hackley, P. C.; Lowers, H. A.; Hill, R. J.; Egenhoff, S. O.; Eberl, D. D.; Blum, A. E. The Nature of Porosity in Organic-Rich Mudstones of the Upper Jurassic Kimmeridge Clay Formation, North Sea, Offshore United Kingdom. *Int. J. Coal Geol.* 2012, 103, 32−50.

(14) Guo, H.; He, R.; Jia, W.; Peng, P. a.; Lei, Y.; Luo, X.; Wang, X.; Zhang, L.; Jiang, C. Pore Characteristics of Lacustrine Shale within the Oil Window in the Upper Triassic Yanchang Formation, Southeastern Ordos Basin, China. *Mar. Pet. Geol.* 2018, 91, 279−296.

(15) Katz, B. J.; Arango, I. Organic Porosity: A Geochemist's View of the Current State of Understanding. *Org. Geochem.* 2018, 123, 1−16.

(16) Milliken, K. L.; Rudnicki, M.; Awwiller, D. N.; Zhang, T. Organic Matter-Hosted Pore System, Marcellus Formation (Devonian), Pennsylvania. *AAPG Bull.* 2013, 97, 177−200.

(17) Pan, L.; Xiao, X.; Tian, H.; Zhou, Q.; Chen, J.; Li, T.; Wei, Q. A Preliminary Study on the Characterization and Controlling Factors of Porosity and Pore Structure of the Permian Shales in Lower Yangtze Region, Eastern China. *Int. J. Coal Geol.* 2015, 146, 68−78.

(18) Schieber, J. Common Themes in the Formation and Preservation of Intrinsic Porosity in Shales and Mudstones—Illustrated with Examples Across the Phanerozoic. *SPE Unconventional Gas Conference*: Pittsburgh, Pennsylvania, USA, 2010.

(19) Wang, F.; Guan, J.; Feng, W.; Bao, L. Evolution of Overmature Marine Shale Porosity and Implication to the Free Gas Volume. *Pet. Explor. Dev.* 2013, 40, 819−824.

(20) Ardakani, O. H.; Sanei, H.; Ghanizadeh, A.; Lavoie, D.; Chen, Z.; Clarkson, C. R. Do All Fractions of Organic Matter Contribute Equally in Shale Porosity? A Case Study from Upper Ordovician Utica Shale, Southern Quebec, Canada. *Mar. Pet. Geol.* 2018, 92, 794−808.

(21) Cavelan, A.; Boussafir, M.; Milbeau, C. L.; Rozenbaum, O.; Laggoun-Défarge, F. Effect of Organic Matter Composition on Source Rock Porosity during Confined Anhydrous Thermal Maturation: Example of Kimmeridge-Clay Mudstones. *Int. J. Coal Geol.* 2019, 212, 103236.

(22) Ko, L. T.; Loucks, R. G.; Milliken, K. L.; Liang, Q.; Zhang, T.; Sun, X.; Hackley, P. C.; Ruppel, S. C.; Peng, S. Controls on Pore Types and Pore-Size Distribution in the Upper Triassic Yanchang Formation, Ordos Basin, China: Implications for Pore-Evolution Models of Lacustrine Mudrocks. *Interpretation* 2017, 5, SF127−SF148.

(23) Loucks, R. G.; Reed, R. M.; Ruppel, S. C.; Hammes, U. Spectrum of Pore Types and Networks in Mudrocks and a Descriptive Classification for Matrix-Related Mudrock Pores. *AAPG Bull.* 2012, 96, 1071−1098.

(24) Mastalerz, M.; Schimmelmann, A.; Drobniak, A.; Chen, Y. Porosity of Devonian and Mississippian New Albany Shale across a Maturation Gradient: Insights from Organic Petrology, Gas Adsorption, and Mercury Intrusion. *AAPG Bull.* 2013, 97, 1621−1643.

(25) Tissot; Welte, D. H. *Petroleum Formation and Occurrence*, 2nd revised and enlarge ed.; Springer Science: Berlin, Heidelberg, 1984.

(26) Wood, J. M.; Sanei, H.; Haeri-Ardakani, O.; Curtis, M. E.; Akai, T. Organic Petrography and Scanning Electron Microscopy Imaging of a Thermal Maturity Series from the Montney Tight-Gas and Hydrocarbon Liquids Fairway. *Bull. Can. Pet. Geol.* **2018**, *66*, 499−515.

(27) Behar, F.; Kressmann, S.; Rudkiewicz, J. L.; Vandenbroucke, M. Experimental Simulation in a Confined System and Kinetic Modelling of Kerogen and Oil Cracking. *Org. Geochem.* **1992**, *19*, 173−189.

(28) Boreham, C. J.; Crick, I. H.; Powell, T. G. Alternative Calibration of the Methylphenanthrene Index against Vitrinite Reflectance: Application to Maturity Measurements on Oils and Sediments. *Org. Geochem.* **1988**, *12*, 289−294.

(29) Landais, P.; Michels, R.; Elie, M. Are Time and Temperature the Only Constraints to the Simulation of Organic Matter Maturation? *Org. Geochem.* **1994**, *22*, 617−630.

(30) Monthioux, M.; Landais, P.; Monin, J.-C. Comparison between Natural and Artificial Maturation Series of Humic Coals from the Mahakam Delta, Indonesia. *Org. Geochem.* **1985**, *8*, 275−292.

(31) Peters, K. E.; Walters, C. C.; Moldowan, J. M. Biomarkers and Isotopes in Petroleum Exploration and Earth History. *Biomarker Guide*; Cambridge University Press: Cambridge, UK; New York, 2005; Vol. 2.

(32) Radke, M. Application of Aromatic Compounds as Maturity Indicators in Source Rocks and Crude Oils. *Mar. Pet. Geol.* **1988**, *5*, 224−236.

(33) Hackley, P. C.; Walters, C. C.; Kelemen, S. R.; Mastalerz, M.; Lowers, H. A. Organic Petrology and Micro-Spectroscopy of Tasmanites Microfossils: Applications to Kerogen Transformations in the Early Oil Window. *Org. Geochem.* **2017**, *114*, 23−44.

(34) Wang, Y.; Liu, L.; Hu, Q.; Hao, L.; Wang, X.; Sheng, Y. Nanoscale Pore Network Evolution of Xiamaling Marine Shale during Organic Matter Maturation by Hydrous Pyrolysis. *Energy Fuels* **2020**, *34*, 1548−1563.

(35) Lewan, M. D. Experiments on the Role of Water in Petroleum Formation. *Geochim. Cosmochim. Acta* **1997**, *61*, 3691−3723.

(36) Michels, R.; Landais, P.; Torkelson, B. E.; Philp, R. P. Effects of Effluents and Water Pressure on Oil Generation during Confined Pyrolysis and High-Pressure Hydrous Pyrolysis. *Geochim. Cosmochim. Acta* **1995**, *59*, 1589−1604.

(37) Ramanampisoa, L.; Disnar, J. R. Primary Control of Paleoproduction on Organic Matter Preservation and Accumulation in the Kimmeridge Rocks of Yorkshire (UK). *Org. Geochem.* **1994**, *21*, 1153−1167.

(38) Boussafir, M.; Gelin, F.; Lallier-Vergès, E.; Derenne, S.; Bertrand, P.; Largeau, C. Electron Microscopy and Pyrolysis of Kerogens from the Kimmeridge Clay Formation, UK: Source Organisms, Preservation Processes, and Origin of Microcycles. *Geochim. Cosmochim. Acta* **1995**, *59*, 3731−3747.

(39) Boussafir, M.; Lallier-Vergès, E.; Bertrand, P.; Badaut-Trauth, D. SEM and TEM Studies on Isolated Organic Matter and Rock Microfacies from a Short-Term Organic Cycle of the Kimmeridge Clay Formation (Yorkshire, GB). *Organic Matter Accumulation*; Springer-Verlag: Berlin, Heidelberg, 1995; pp 15−30.

(40) Desprairies, A.; Bachaoui, M.; Ramdani, A.; Tribovillard, N. Clay Diagenesis in Organic-Rich Cycles from the Kimmeridge Clay Formation of Yorshire (G.B.): Implication for Palaeoclimatic Interpretations. *Organic Matter Accumulation*; Springer Berlin Heidelberg: Berlin, Heidelberg, 1995; pp 63−91.

(41) Ramanampisoa, L. R.; Radke, M. Extractable Aromatic Hydrocarbons in a Short-Term Organic Cycle of the Kimmeridge Clay Formation, Yorkshire (U.K.): Relationship to Primary Production and Thermal Maturity. *Org. Geochem.* **1995**, *23*, 803−817.

(42) Boussafir, M.; Lallier-Vergès, E. Accumulation of Organic Matter in the Kimmeridge Clay Formation (KCF): An Update Fossilisation Model for Marine Petroleum Source-Rocks. *Mar. Pet. Geol.* **1997**, *14*, 75−83.

(43) Cavelan, A.; Boussafir, M.; Rozenbaum, O.; Laggoun-Défarge, F. Organic Petrography and Pore Structure Characterization of Low-Mature and Gas-Mature Marine Organic-Rich Mudstones: Insights

into Porosity Controls in Gas Shale Systems. *Mar. Pet. Geol.* **2019**, *103*, 331−350.

(44) Oschmann, W. Kimmeridge Clay Sedimentation—A New Cyclic Model. *Palaeogeogr., Palaeoclimatol., Palaeoecol.* **1988**, *65*, 217−251.

(45) Lallier-Vergès, E.; Bertrand, P.; Tribovillard, N.; Desprairies, A. Short-Term Organic Cyclicities from the Kimmeridge Clay Formation of Yorkshire (G.B.): Combined Accumulation and Degradation of Organic Carbon under the Control of Primary Production Variations. *Organic Matter Accumulation*; Springer: Berlin, Heidelberg, 1995; pp 3−13.

(46) Uliana, M. A.; Legarreta, L.; Laffitte, G. A.; Villar, H. J. Estratigrafía y Geoquímica de Las Facies Generadoras de Hidrocarburos En Las Cuencas Petrolíferas de Argentina. *Actas IV Congreso de Exploración y Desarrollo de Hidrocarburos*: Argentina, 1999.

(47) Legarreta, L.; Villar, H. J. *The Vaca Muerta Formation (Late Jurassic—Early Cretaceous), Neuquén Basin, Argentina: Sequences, Facies and Source Rock Characteristics*; Unconventional Resources Technology Conference: San Antonio, Texas, USA, 2015.

(48) Espitalie, J.; Deroo, G.; Marquis, F. La pyrolyse Rock-Eval et ses applications. Première partie. *Rev. Inst. Fr. Pét.* **1985**, *40*, 563−579.

(49) Espitalie, J.; Deroo, G.; Marquis, F. La pyrolyse Rock-Eval et ses applications. Deuxième partie. *Rev. Inst. Fr. Pét.* **1985**, *40*, 755−784.

(50) Lafargue, E.; Marquis, F.; Pillot, D. Rock-Eval 6 Applications in Hydrocarbon Exploration, Production, and Soil Contamination Studies. *Rev. Inst. Fr. Pét.* **1998**, *53*, 421−437.

(51) Radke, M.; Welte, D. H.; Willsch, H. Maturity Parameters Based on Aromatic Hydrocarbons: Influence of the Organic Matter Type. *Org. Geochem.* **1986**, *10*, 51−63.

(52) Bertrand, P.; Bordenave, M. L.; Brosse, E.; Espitalié, J.; Houzay, J. P.; Pradier, B.; Vandenbroucke, M.; Walgenwitz, F. Other Methods and Tools for Source Rock Appraisal. *Applied Petroleum geochemistry*; Bordenave M.L., 1993; Vol. 525, pp 279−371.

(53) Robert, P. Etude Pétrographique Des Matières Organiques Insolubles Par La Mesure de Leur Pouvoir Réflecteur: Contribution à l'exploration Pétrolière et à La Connaissance Des Bassins Sédimentaires. *Rev. Inst. Fr. Pet. Ann. Combust. Liq.* **1971**, *26*, 104−135.

(54) Barrett, E. P.; Joyner, L. G.; Halenda, P. P. The Determination of Pore Volume and Area Distributions in Porous Substances. I. Computations from Nitrogen Isotherms. *J. Am. Chem. Soc.* **1951**, *73*, 373−380.

(55) Okiongbo, K. S.; Aplin, A. C.; Larter, S. R. Changes in Type II Kerogen Density as a Function of Maturity: Evidence from the Kimmeridge Clay Formation. *Energy Fuels* **2005**, *19*, 2495−2499.

(56) Michels, R.; Landais, P.; Philp, R. P.; Torkelson, B. E. Effects of Pressure on Organic Matter Maturation during Confined Pyrolysis of Woodford Kerogen. *Energy Fuels* **1994**, *8*, 741−754.

(57) Sing, K. S. W. Reporting physisorption data for gas/solid systems with special reference to the determination of surface area and porosity (Recommendations 1984). *Pure Appl. Chem.* **1985**, *57*, 603−619.

(58) Shanmugam, G. Significance of Coniferous Rain Forests and Related Organic Matter in Generating Commercial Quantities of Oil, Gippsland Basin, Australia. *AAPG Bull.* **1985**, *69*, 1241−1254.

(59) Isaksen, G. H.; Ledje, K. H. Source Rock Quality and Hydrocarbon Migration Pathways within the Greater Utsira High Area, Viking Graben, Norwegian North Sea. *AAPG Bull.* **2001**, *85*, 861.

(60) van Graas, G. W. Biomarker Maturity Parameters for High Maturities: Calibration of the Working Range up to the Oil/Condensate Threshold. *Org. Geochem.* **1990**, *16*, 1025−1032.

(61) Orr, W. L. Comments on Pyrolytic Hydrocarbon Yields in Source-Rock Evaluation. *Advances in Organic Geochemistry*; Wiley & Sons Ltd., 1981.

(62) Huang, Y.; Street-Perrott, F. A.; Perrott, R. A.; Metzger, P.; Eglinton, G. Glacial−Interglacial Environmental Changes Inferred from Molecular and Compound-Specific δ13C analyses of sediments

from Sacred Lake, Mt. Kenya. *Geochim. Cosmochim. Acta* **1999**, *63*, 1383−1404.

(63) Ficken, K. J.; Li, B.; Swain, D. L.; Eglinton, G. An N-Alkane Proxy for the Sedimentary Input of Submerged/floating Freshwater Aquatic Macrophytes. *Org. Geochem.* **2000**, *31*, 745−749.

(64) Huang, W.-Y.; Meinschein, W. G. Sterols as Ecological Indicators. *Geochim. Cosmochim. Acta* **1979**, *43*, 739−745.

(65) Jubb, A. M.; Hackley, P. C.; Hatcherian, J. J.; Qu, J.; Nesheim, T. O. Nanoscale Molecular Fractionation of Organic Matter within Unconventional Petroleum Source Beds. *Energy Fuels* **2019**, *33*, 9759−9766.

(66) Chakhmakhchev, A.; Suzuki, M.; Takayama, K. Distribution of Alkylated Dibenzothiophenes in Petroleum as a Tool for Maturity Assessments. *Org. Geochem.* **1997**, *26*, 483−489.

(67) Tissot, B. Utilisation Des Alcanes Comme Fossiles Géochimiques Indicateurs Des Environnements Géologiques. *Advance in Organic geochemistry*; Enadimsa, 1977; Vol. *1975*, pp 117−154.

(68) Hackley, P. C.; Cardott, B. J. Application of Organic Petrography in North American Shale Petroleum Systems: A Review. *Int. J. Coal Geol.* **2016**, *163*, 8−51.

(69) Hackley, P. C. Application of Organic Petrology in High Maturity Shale Gas Systems. *Role of Organic Petrology in the Exploration of Conventional and Unconventional Hydrocarbon Systems*; Bentham Science Publishers, 2017, Vol. *1*, pp 205−235.

(70) Song, L.; Martin, K.; Carr, T. R.; Ghahfarokhi, P. K. Porosity and Storage Capacity of Middle Devonian Shale: A Function of Thermal Maturity, Total Organic Carbon, and Clay Content. *Fuel* **2019**, *241*, 1036−1044.

(71) Jarvie, D. M.; Hill, R. J.; Ruble, T. E.; Pollastro, R. M. Unconventional Shale-Gas Systems: The Mississippian Barnett Shale of North-Central Texas as One Model for Thermogenic Shale-Gas Assessment. *AAPG Bull.* **2007**, *91*, 475−499.

(72) Waples, D. W.; Marzi, R. W. The Universality of the Relationship between Vitrinite Reectance and Transformation Ratio. *Org. Geochem.* **1988**, *28*, 383−388.

(73) Landais, P. Assessment of Coal Potential Evolution by Experimental Simulation of Natural Coalification. *Org. Geochem.* **1991**, *17*, 705−710.

(74) Guo, H.; Jia, W.; Peng, P. a.; Zeng, J.; He, R. Evolution of Organic Matter and Nanometer-Scale Pores in an Artificially Matured Shale Undergoing Two Distinct Types of Pyrolysis: A Study of the Yanchang Shale with Type II Kerogen. *Org. Geochem.* **2017**, *105*, 56−66.

(75) Liu, Y.; Xiong, Y.; Li, Y.; Peng, P. A. Effect of Thermal Maturation on Chemical Structure and Nanomechanical Properties of Solid Bitumen. *Mar. Pet. Geol.* **2018**, *92*, 780−793.

(76) Lewan, M. D. Laboratory Simulation of Petroleum Formation. *Org. Geochem.* **1993**, *11*, 419−442.

(77) Behar, F.; Lewan, M. D.; Lorant, F.; Vandenbroucke, M. Comparison of Artificial Maturation of Lignite in Hydrous and Nonhydrous Conditions. *Org. Geochem.* **2003**, *34*, 575−600.

(78) Huang, W.-L. Experimental Study of Vitrinite Maturation: Effects of Temperature, Time, Pressure, Water, and Hydrogen Index. *Org. Geochem.* **1996**, *24*, 233−241.

(79) Monthioux, M. Expected Mechanisms in Nature and in Confined-System Pyrolysis. *Fuel* **1988**, *67*, 843−847.